SEISMIC RESPONSE STUDY OF THE

HWY 101/PAINTER STREET OVERPASS NEAR

EUREKA USING STRONG-MOTION RECORDS

by

Rakesh K. Goel and Anil K. Chopra

Department of Civil Engineering
University of California, Berkeley

DIVISION OF MINES AND GEOLOGY
JAMES F. DAVIS
STATE GEOLOGIST

DISCLAIMER

The content of this report was developed under Contract No. 1092-545 from the Strong Motion Instrumentation Program in the Division of Mines and Geology of the California Department of Conservation. This report has not been edited to the standards of a formal publication. Any opinions, findings, conclusions or recommendations contained in this report are those of the authors, and should not be interpreted as representing the official policies, either expressed or implied, of the State of California.

SEISMIC RESPONSE STUDY OF THE

HWY 101/PAINTER STREET OVERPASS NEAR

EUREKA USING STRONG-MOTION RECORDS

by

Rakesh K. Goel and Anil K. Chopra

Department of Civil Engineering
University of California
Berkeley, California 94720

Data Utilization Report CSMIP/95-01

California Strong Motion Instrumentation Program

March 1995

California Department of Conservation
Division of Mines and Geology
Office of Strong Motion Studies
801 K Street, MS 13-35
Sacramento, California 95814-3531

PREFACE

The California Strong Motion Instrumentation Program (CSMIP) in the Division of Mines and Geology of the California Department of Conservation promotes and facilitates the improvement of seismic codes through the Data Interpretation Project. The objective of the this project is to increase the understanding of earthquake strong ground shaking and its effects on structures through interpretation and analysis studies of CSMIP and other applicable strong motion data. The ultimate goal is to accelerate the process by which lessons learned from earthquake data are incorporated into seismic code provisions and seismic design practices.

The specific objectives of the CSMIP Data Interpretation Project are to:

1. Understand the spatial variation and magnitude dependence of earthquake strong ground motion.

2. Understand the effects of earthquake motions on the response of geologic formations, buildings and lifeline structures.

3. Expedite the incorporation of knowledge of earthquake shaking into revision of seismic codes and practices.

4. Increase awareness within the seismological and earthquake engineering community about the effective usage of strong motion data.

5. Improve instrumentation methods and data processing techniques to maximize the usefulness of SMIP data. Develop data representations to increase the usefulness and the applicability to design engineers.

This report is the eleventh in a series of CSMIP data utilization reports designed to transfer recent research findings on strong-motion data to practicing seismic design professionals and earth scientists. CSMIP extends its appreciation to the members of the Strong Motion Instrumentation Advisory Committee and its subcommittees for their recommendations regarding the Data Interpretation Research Project.

Anthony F. Shakal
CSMIP Program Manager

Moh J. Huang
CSMIP Data Interpretation
Project Manager

ABSTRACT

A procedure is developed to estimate the stiffness of abutment-soil systems directly from the earthquake motions of small, well-instrumented bridges using a simple equilibrium-based approach without finite-element modeling of the structure or the abutment-soil systems. This procedure is used to estimate abutment stiffnesses of the US 101/Painter Street Overpass during past earthquakes. The calculated abutment stiffnesses, which include the effects of soil-structure interaction and nonlinear behavior of the soil, are used to investigate effects of abutment deformation on the abutment stiffness during an earthquake and to explain the torsional motions of the road deck. It is demonstrated that the abutment stiffness decreases significantly at larger deformations. The torsional motions of the road deck resulted, in part, because of the differences in transverse stiffnesses of the two abutments. Also evaluated are the CALTRANS, AASHTO-83, and ATC-6 procedures for estimating the abutment stiffness. The CALTRANS procedure leads to a good estimate of the stiffness along the abutment (transverse to the deck) provided the deformation assumed in computing the stiffness is close to the actual deformation during an earthquake. However, this procedure leads to overestimation of the stiffness normal to the abutment (along the length of the deck). The AASHTO-83 and ATC-6 procedures give an initial estimate of the abutment stiffness that is too high in both directions.

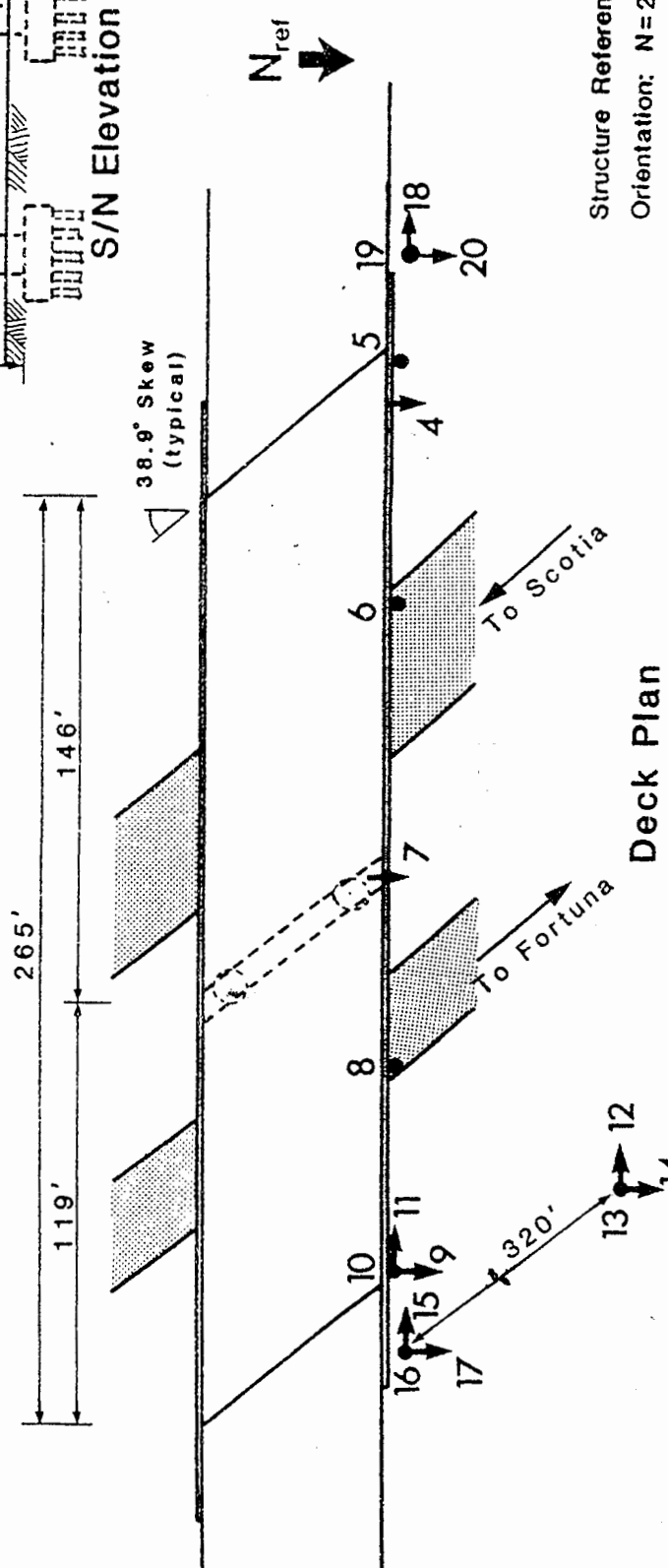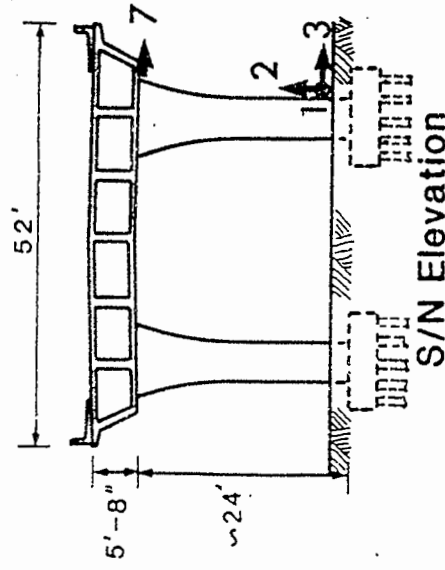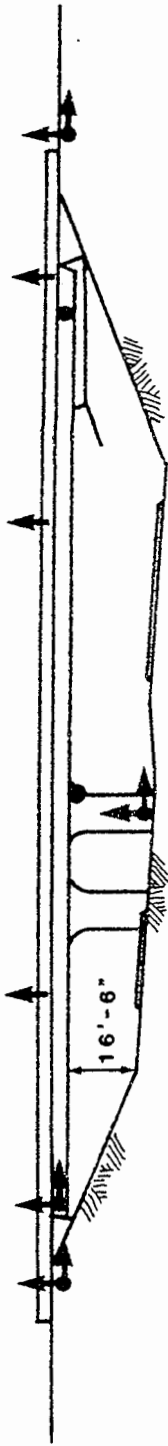# ACKNOWLEDGMENTS

TABLE OF CONTENTS

INTRODUCTION

Most specifications and guidelines for earthquake design of highway bridges require that the abutment-soil systems be included in the structural idealization as equivalent discrete springs (CALTRANS, 1989; ATC-6, 1981; AASHTO-83, 1988). The spring stiffness is usually calculated using some simplified rules and an iterative process. It is not clear how well this stiffness value represents the complex behavior of abutment-soil systems, which is influenced by soil-structure interaction and nonlinear behavior of the soil. Obviously, it would be useful to compare the design value of abutment-soil stiffness with its value determined directly from motions recorded at bridges during earthquakes.

Several previous investigators have attempted to estimate the stiffness values of abutment-soil systems. For example, Wilson (1988) and Levine and Scott (1989) proposed theoretical models for determining the abutment stiffness of non-skewed bridges. In these investigations, the abutment stiffness is calculated from the soil properties and abutment dimensions. Others attempted to determine the stiffness values either from free or forced vibration tests (Crouse et al., 1979; Douglas et al., 1990) or from motions recorded during earthquakes (Romstad and Maroney, 1990; Sweet and Morill, 1993). In these studies, properties of a finite-element model of the structure and the abutment-soil systems are adjusted till calculated vibration properties -- natural frequencies and modes -- and/or motions match the recorded data.

In this investigation, a procedure is developed to estimate stiffness of abutment-soil systems directly from the motions of small, well-instrumented bridges recorded during earthquakes. A structure that provides such an opportunity is the US 101/Painter Street Overpass (Figure 1) where motions at three locations on the deck have been recorded during several past earthquakes. An idealization of this structural system contains three unknown stiffness parameters -- springs along the east abutment, normal to the east abutment, and along the west abutment. For simplicity, the stiffness values of two columns in the central bent are assumed to be known and are determined from their structural details. The unknown stiffness parameters are defined by the

Rio Dell - Hwy 101/Painter Street Overpass
(CSMIP Station No. 89324)

SENSOR LOCATIONS

E/W Elevation

16'-6"

S/N Elevation

52'

5'-8"   ~24'

1 2 3 7

Deck Plan

265'

146'   119'

38.9° Skew (typical)

10 11 9 5 19 18 20 4 6 8 7 12 14 13

320'

16 15 17

N_{ref}

To Scotia

To Fortuna

Structure Reference
Orientation: N = 2°

Figure 1. US 101/Painter Street Overpass: structural details and sensor locations (Shakal et al., 1992)

force-deformation relations for abutment-soil systems, which are determined from the recorded motions using the dynamic equilibrium of the road deck. The abutment stiffnesses thus obtained include all effects, including those of soil-structure interaction and nonlinear behavior of the soil. These data provide a basis to (1) investigate the effects of abutment deformation on the abutment stiffness and to explain the torsional motions of the road deck recorded during past earthquakes, and (2) evaluate the CALTRANS, AASHTO-83, and ATC-6 procedures for estimating the abutment stiffness.

STRUCTURE AND RECORDED MOTIONS

The US 101/Painter Street Overpass, shown in Figure 1, is located in Rio Dell, California (Shakal et al., 1992). This 265 ft long bridge consists of a continuous reinforced-concrete (R/C) multi-cell box-girder road deck supported on integral abutments at the two ends and on an R/C two-column bent. The bent divides the bridge into two unequal spans of 119 ft and 146 ft. Both abutments and bent are skewed at an angle of 38.9°. The east abutment is monolithic with the superstructure and is supported on 14 driven 45-ton concrete friction piles. The west abutment rests on a neoprene bearing strip that is part of a designed thermal expansion joint of the road deck. The foundation of this abutment consists of 16 driven 45-ton concrete friction piles. This bridge is typical of short bridges in California spanning two or four lane separated highways.

The US 101/Painter Street Overpass was instrumented by California Strong Motion Instrumentation Program (CSMIP) in 1977. Figure 1 also shows locations of the sensors and identifies the channels on this structure; a detailed description of these data channels is included in Appendix A. Since this overpass was instrumented, it has yielded strong motion records during nine earthquakes (Table 1). Since the first three of these earthquakes did not yield data at all locations, they are not considered in this investigation. From the remaining six, we have selected motions recorded during two earthquakes: the main shock of the April 25, 1992, Cape Mendocino/Petrolia earthquake and the second event of the November 21, 1986, Cape Mendocino earthquake. The first of these two earthquakes is included as an infrequent large event representing the design earthquake and the latter is considered as a frequent small event representing the service level earthquake. The remaining four earthquakes are not considered for the following reason. Since the motions during the first aftershock of Cape Mendocino/Petrolia earthquake on April 26, 1992 are similar to those during the first of the two selected earthquakes, the results are expected to be similar for the two earthquakes. For the same reason, results for the remaining three earthquakes are expected to be similar to the second of the two selected earthquakes.

Figures 2 and 3 show the horizontal components of the accelerations recorded at three locations on the road deck -- channels 4, 7, and 9 in direction transverse to the deck and channel 11 in the longitudinal direction. Also shown are the free-field motions recorded by channel 14 in the transverse direction and channel 12 in the longitudinal direction; details on the location coordinates of these data channels are included in Appendix A. During the 1992 earthquakes, the peak free-field accelerations were 0.380g and 0.543g in the longitudinal and transverse directions respectively. These motions were amplified to 0.452g in the longitudinal direction near the east end of the road deck and 1.089g in the transverse direction near the west end of the road deck. The 1986 earthquake caused much smaller free-field motions of 0.144g and 0.116g in the longitudinal and transverse directions that were amplified to 0.183g and 0.350g in the longitudinal and transverse directions, respectively.

Table 1. List of recorded motions at the US 101/Painter Street Overpass

| No.	Earthquake	Depth (Km.)	Mag. M_L	Dist. (Km.)	Max. Hor. FF Acc.(g)	Max. Hor. Str. Acc.(g)
1.	Trinidad Offshore 8 Nov, 1980	19	6.9	82	0.147	0.169
2.	Rio Dell 16 Dec, 1982	5	4.4	15	--	0.420
3.	Eureka 24 Aug, 1983	30	5.5	61	--	0.215
4.	Cape Mendocino 21 Nov, 1986 (First Event)	17	5.1	32	0.432	0.399
5.	Cape Mendocino 21 Nov, 1986 (Second Event)	18	5.1	26	0.144	0.350
6.	Cape Mendocino 31 Jul, 1987	17	5.5	28	0.141	0.335
7.	Cape Mendocino/Petrolia 25 Apr, 1992	15	6.4	24	0.543	1.089
8.	Cape Mendocino/Petrolia 26 Apr, 1992 (AS # 1)	18	6.2	42	0.516	0.757
9.	Cape Mendocino/Petrolia 26 Apr, 1992 (AS # 2)	21	6.4	41	0.262	0.311
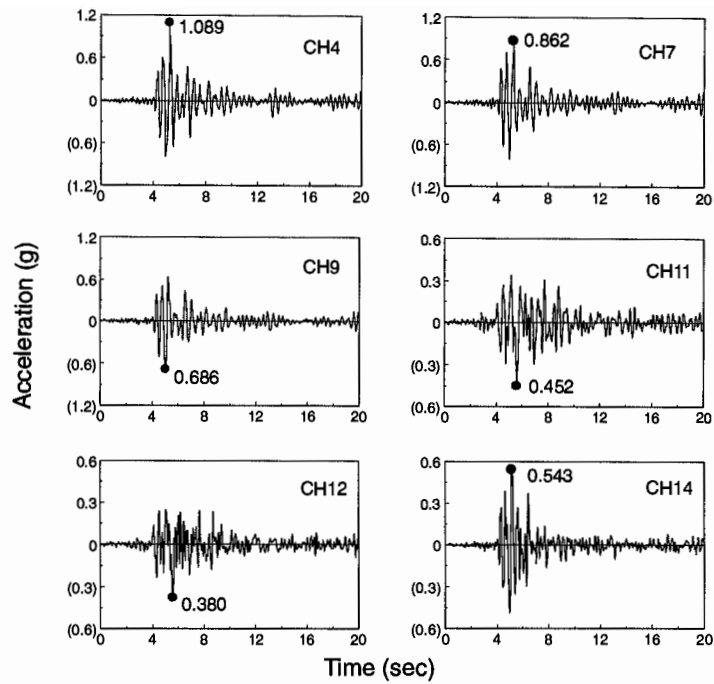
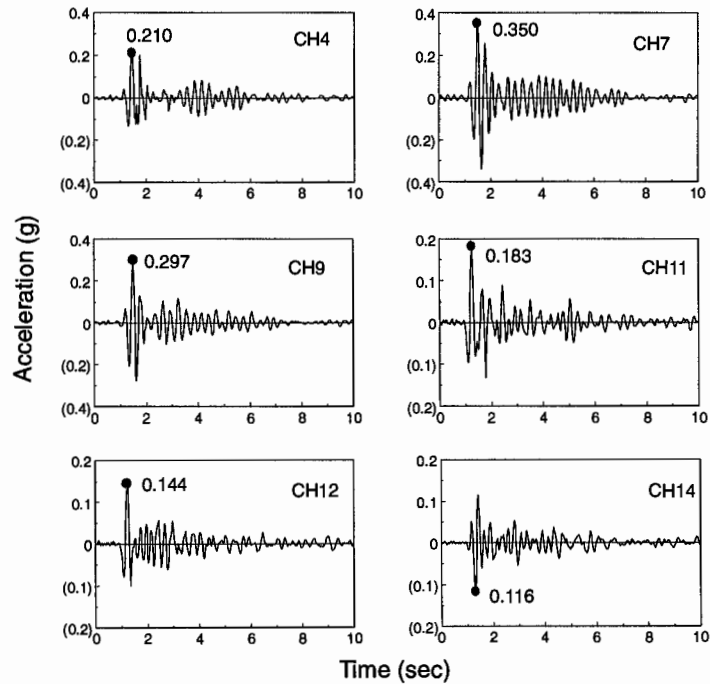Figure 2. Accelerations recorded during the 1992 Cape Mendocino/Petrolia earthquake

Figure 3. Accelerations recorded during the 1986 Cape Mendocino earthquake

7

ANALYSIS PROCEDURE

Structural Idealization

Figure 4 shows an idealized model of the US 101/Painter Street Overpass. The model consists of the road deck with three spring-damper systems, which represent the stiffness and damping properties of abutment-soil systems along the east abutment, normal to the east abutment, and along the west abutment. The spring represents the stiffness property and the damper accounts for material and radiation damping of the abutment-soil system. Each column in the central bent is represented by two linear elastic springs -- one normal to and other along the bent; no damper is included because the energy dissipation is primarily at the abutments. Furthermore, the columns are assumed to response in the linear elastic range because no cracking was observed in the columns even after the strongest shaking of the April 25, 1992, Cape Mendocino/Petrolia earthquake.

Equations of Equilibrium

Figure 5 shows the free-body diagram for structural idealization of Figure 4. The three equations of dynamic equilibrium for this system in the x, y, and θ directions are:

$$\mathbf{f}_I + \mathbf{f}_D + \mathbf{f}_S = \mathbf{0} \tag{1}$$

in which $\mathbf{f}_I^T = \langle f_{Ix},\ f_{Iy},\ f_{I\theta}\rangle$ is the vector of inertia forces, $\mathbf{f}_D$ is the vector of damping forces, and $\mathbf{f}_S$ is the vector of spring forces; $\mathbf{f}_D$ and $\mathbf{f}_S$ are formed by appropriately transforming forces at the abutments: $(f_{D1} + f_{S1})$, $(f_{D2} + f_{S2})$, and $(f_{D3} + f_{S3})$; and the forces at the columns: f_{S4}, f_{S5}, f_{S6}, and f_{S7} to the x, y, and θ coordinate system.
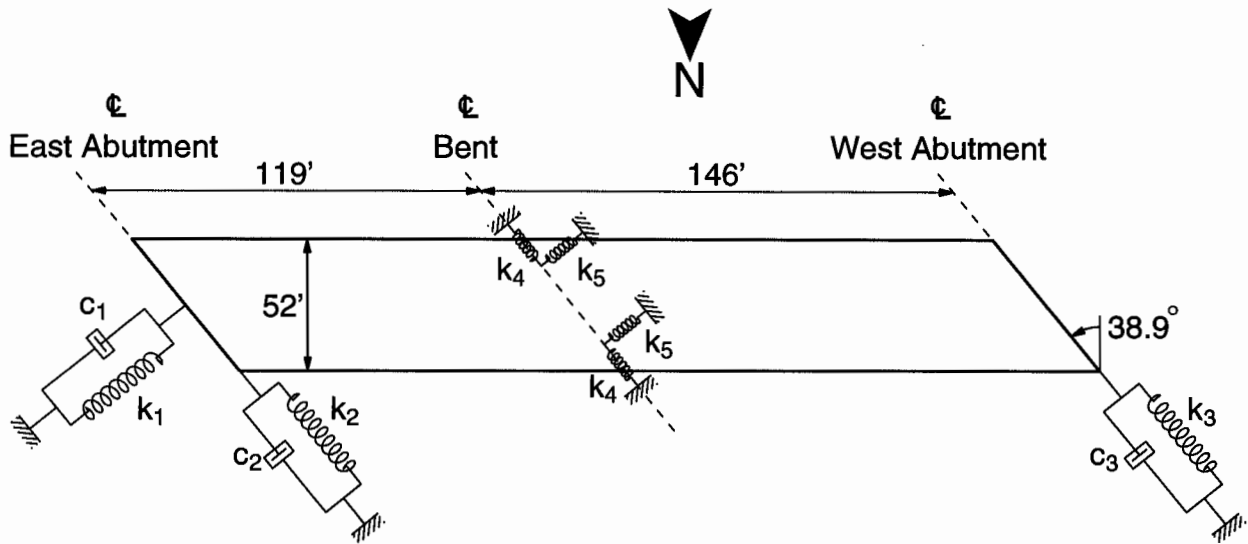
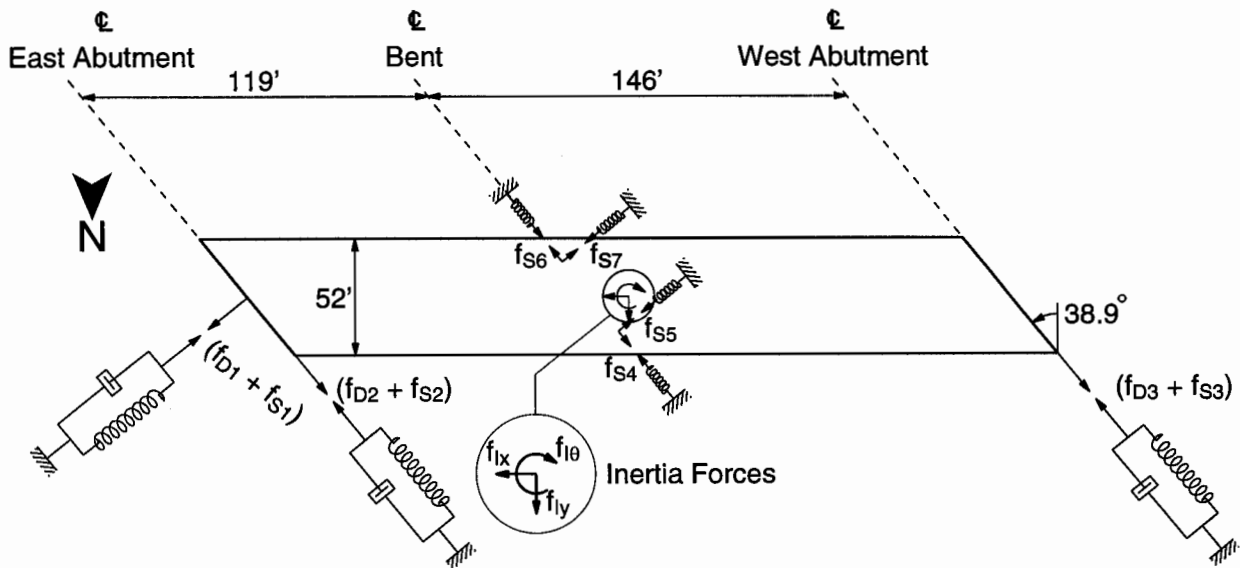Figure 4. Idealized model of US 101/Painter Street Overpass

Figure 5. Free-body diagram for structural idealization of US 101/Painter Street Overpass

9

Abutment Forces and Deformations

The only unknowns in equation (1) are the abutment forces, which are determined by solving the three equations at each instant of time. The three components of the inertia force vector are computed from the mass properties and recorded accelerations. The force in each column spring is determined from its known stiffness and deformation. The procedures to calculate the inertia forces and column spring forces are included in Appendices C and D, respectively.

At each time-instant the deformation in the spring-damper system modeling the abutment-soil system or the column spring is obtained by subtracting the free-field motion from the motion at the top of the abutment or the column respectively; the latter can be computed from recorded motions of the road deck by the procedure presented in Appendix B.

Based on the locations of accelerometers shown in Figure 1, it appears that motions at the base of the column are available, recorded by sensors 1 to 3, and therefore may be used as the input motion to the column. However, field inspection of the structure revealed that these sensors are located about 3 ft above the ground level. Assuming that the top of the pile cap supporting the column is about 3 ft below the ground level, the location of the sensors is about 6 ft above the column base. Thus the sensors record motions at about one-quarter the column height of 24 ft (Figure 1) and not at the base of the column.

Abutment Stiffness

Solution of the three algebraic equations (1) at each time instant leads to the abutment forces which are plotted against the computed displacements to obtain Figures 6 and 7. The stiffness of the abutment-soil system is determined by isolating individual loops from Figures 6 and 7. Two such loops are shown in Figure 8 -- one isolated from Figure 7b and the other from Figure 6c. The nearly elliptical shape of the force-deformation relation for the abutment-soil system along the east abutment (Figure 8a) suggests linear viscoelastic behavior. The spring stiffness is the slope of the major axis of the ellipse; the two plausible axis shown in Figure 8a indicate stiffness values of 29151 and 26000 kips/ft. Unlike the previous loop, which suggests linear behavior of the system during the smaller earthquake, the loop shown in Figure 8b during the large earthquake exhibits

10

significant nonlinearity as evident from the elasto-plastic force-deformation behavior with strain hardening. From such loops, the upper and lower bounds of the stiffness can be estimated from the secant slopes: 7500 and 12000 kips/ft for the positive and negative deformations, respectively.
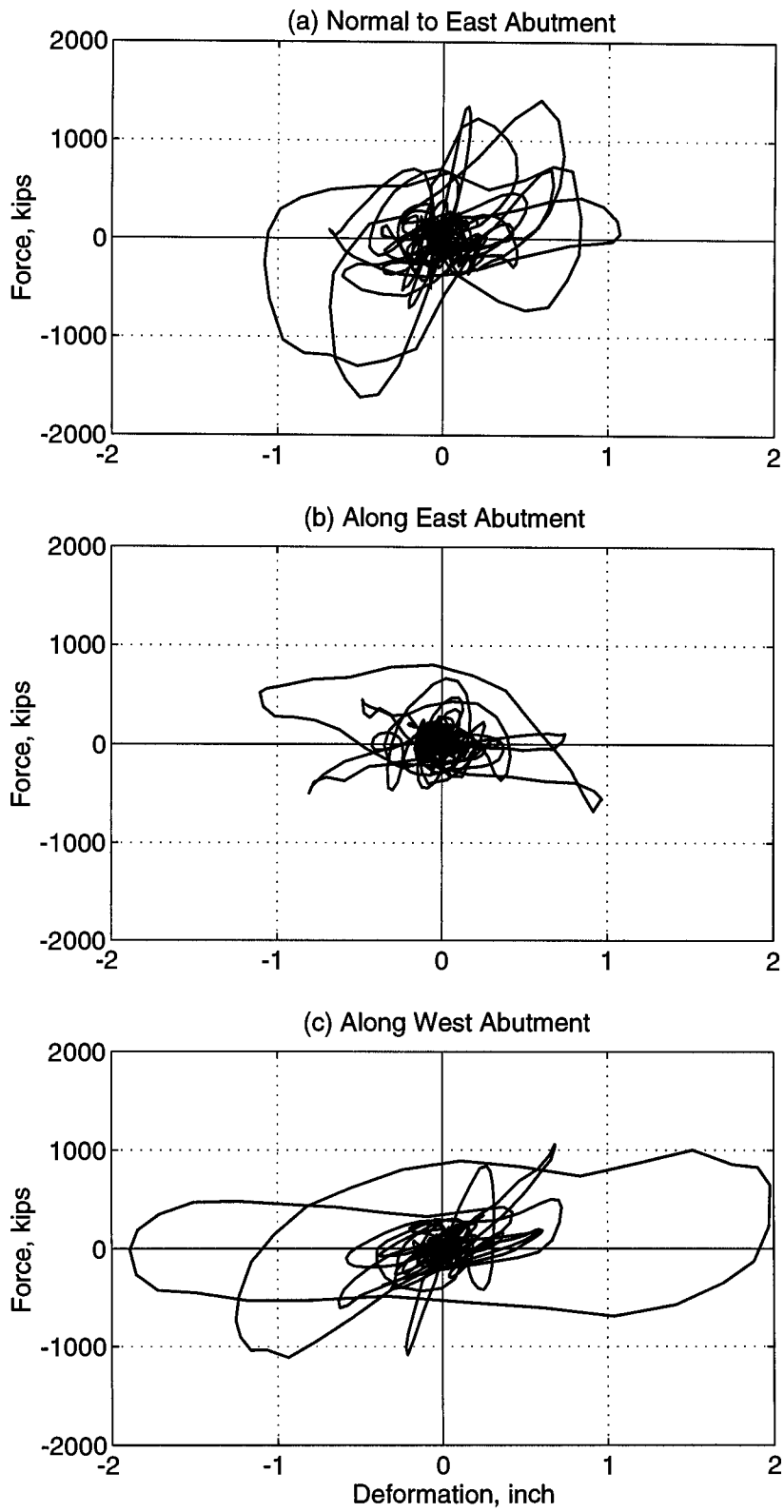
Figure 6. Force-deformation relationships of the abutments during the 1992 earthquake
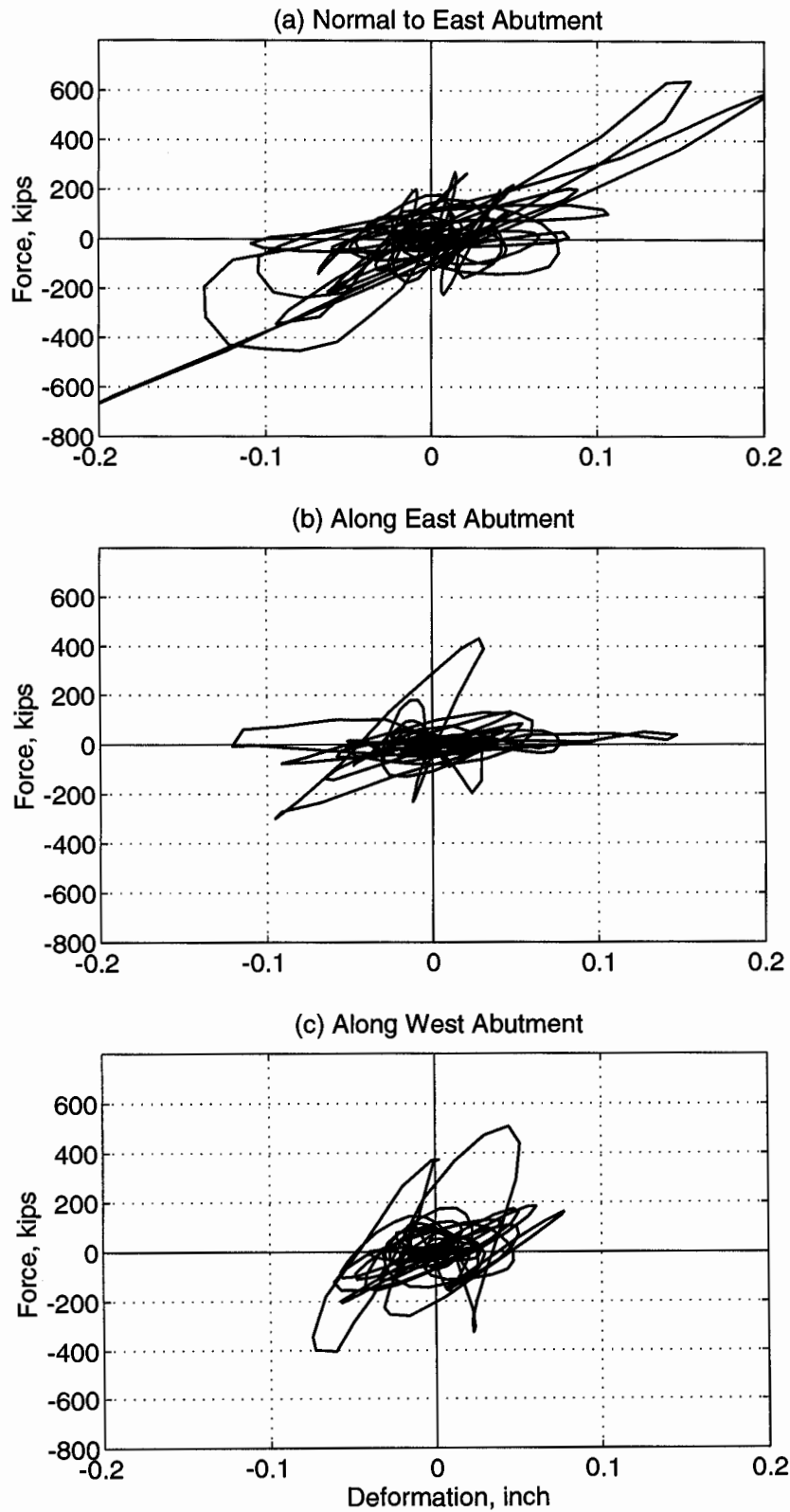
12

Figure 7. Force-deformation relationships of the abutments during the 1992 earthquake
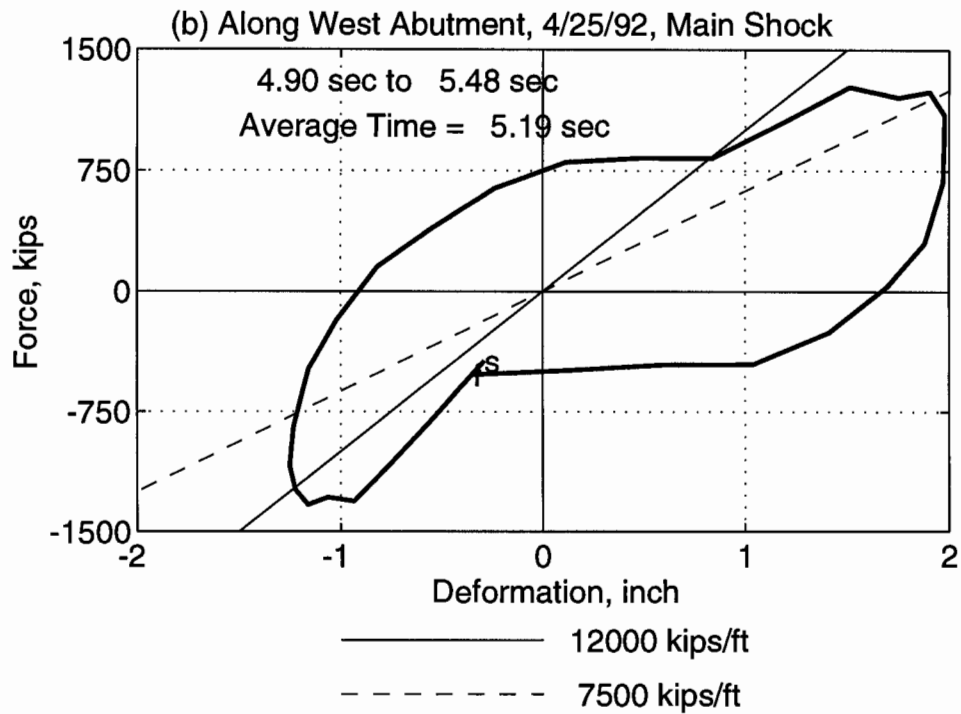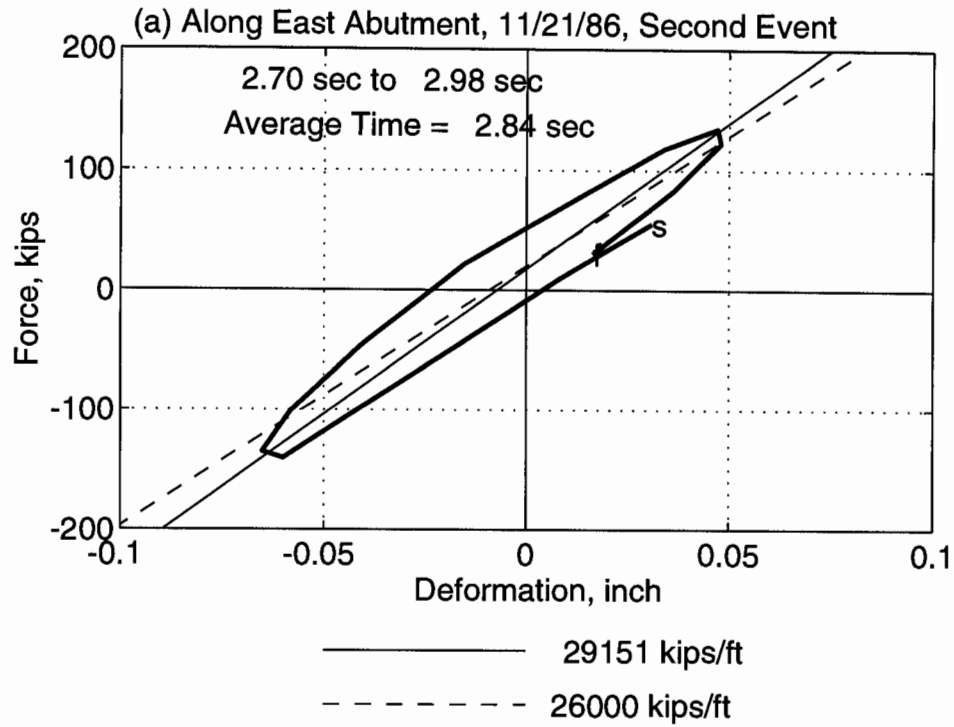
Figure 8. Individual loops isolated from force-deformation relationships of abutments

EFFECTS OF ABUTMENT DEFORMATION ON ABUTMENT STIFFNESS

How the total abutment deformation influences the abutment stiffness is investigated next; the total abutment deformation during a single hysteresis loop is defined as the sum of the deformation amplitudes in the positive and negative directions of the loop. For this purpose examined first is the time-variation of abutment deformation and stiffness during the 1992 earthquake followed by the time-variation of the abutment stiffness during the intense shaking of the 1992 earthquake and the much smaller shaking of the 1986 earthquake.

Time-Variation of Abutment Deformation and Stiffness

Figure 9 shows the time-variation of the abutment stiffness (solid circles) with its scale on the left hand side and of the total deformation (open circles) with its scale on the right hand side; the upper and lower bounds of the stiffness are connected by a vertical line. The results are for the main shock of the 1992 Cape Mendocino/Petrolia earthquake. To obtain this figure the upper and lower bound values of the stiffness and the total deformation determined from a hysteresis loop, as described in the preceding section, were plotted at time corresponding to middle of the loop; further details of the procedure used are available in Appendix E. It is clear from these results that the abutment stiffness varies significantly during the same earthquake. This variation is particularly large for the stiffness normal to the east abutment (Figure 9a). The abutment deformation also varies significantly during the earthquake: deformation is small during the initial build-up phase of the shaking, increases as the amplitude of the motion increases during the strong motion phase, and becomes small as the motion becomes less intense during the later part of shaking.

By examining the deformation along with the stiffness, presented in Figure 9, the following general pattern emerges:

- The abutment tends to be stiff for the smaller deformations during the build-up phase of the shaking.

- The stiffness of abutment decreases as its deformation increases during the stronger motions.

- The abutment recovers some of its stiffness with subsequent reduction in its deformation as the motion becomes less intense towards the later part of the shaking.

- The stiffness recovery is only partial: the stiffness for a deformation level may not return to the value prior to a large deformation cycle. This recovery is gradual over time and is especially slow after repeated large deformation cycles.

This abutment behavior indicates that soil enclosed between the wingwalls provides significant resistance to the abutment motion for small deformation levels. For larger deformations, however, the soil becomes less effective. The reduction in stiffness for large deformation is also partly due to the nonlinear behavior of the soil apparent from hysteresis loops of Figures 6 and 8b.

Time-Variation of Abutment Stiffness During Two Earthquakes

Figure 10 compares the abutment stiffness values during the intense shaking of the 1992 earthquake and the much smaller motions of the 1986 earthquake. These results show that the abutment behavior is consistent with the trends identified in the previous section. The abutment is generally less stiff during the 1992 earthquake (Figures 10a and 10c) because of larger abutment deformations resulting from more intense shaking during this earthquake; during this earthquake, the peak abutment deformations are almost ten times those during the 1986 earthquake (Figure 6 and 7). This effect is more pronounced for the west abutment because of its larger deformations resulting from torsional motions of the road deck during the 1992 earthquake (Figure 6c). If the deformations during the two earthquakes are similar, as in the transverse direction at the east abutment, the abutment stiffnesses are also similar (Figure 10b).
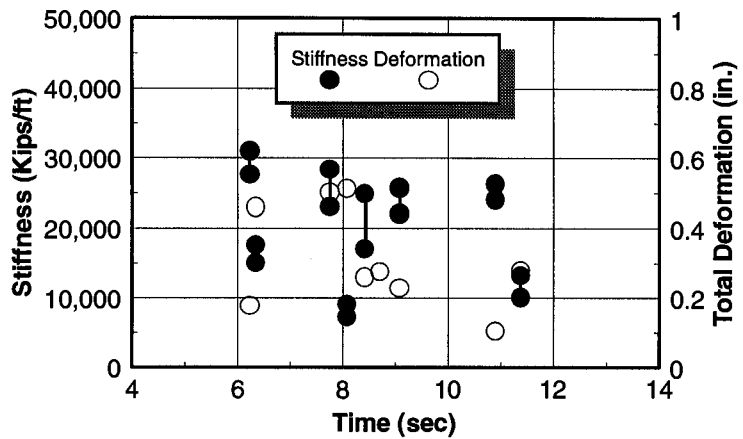
(a) Normal to East Abutment
4/25/92, Main Shock
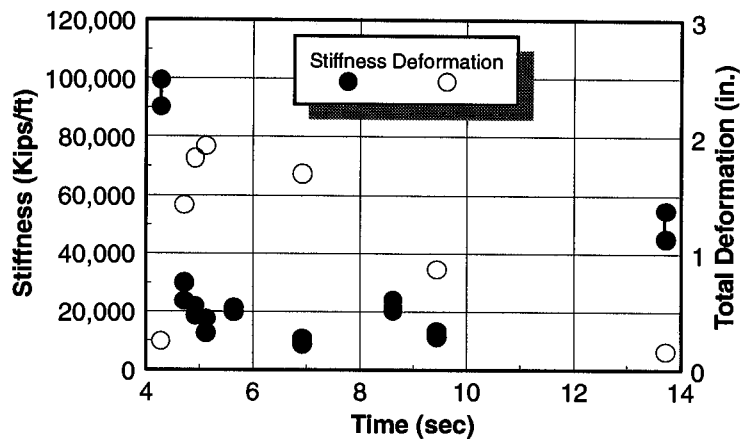
(b) Along East Abutment
4/25/92, Main Shock

(c) Along West Abutment
4/25/92, Main Shock
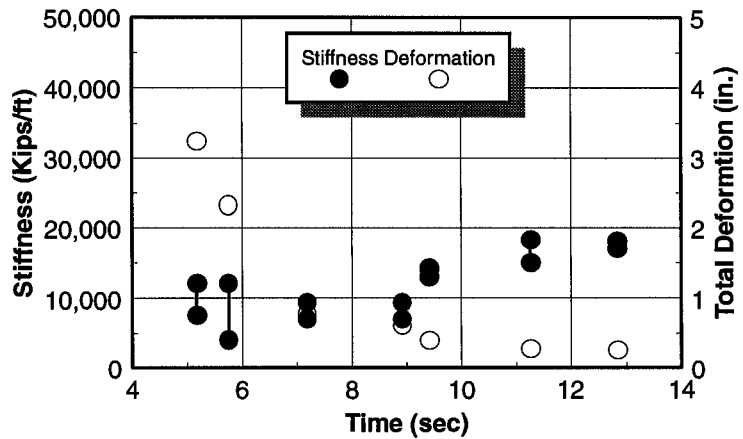
Figure 9. Time-variation of abutment deformation and stiffness

17

(a) Normal to East Abutment

4/25/92 Main Shock ● 11/21/86 Second Event ○

Figure: scatter plot, Stiffness (Kips/ft) vs Time (sec)

(b) Along East Abutment

4/25/92 Main Shock ● 11/21/86 Second Event ○

Figure: scatter plot, Stiffness (Kips/ft) vs Time (sec)

(c) Along West Abutment

4/25/92 Main Shock ● 11/21/86 Second Event ○

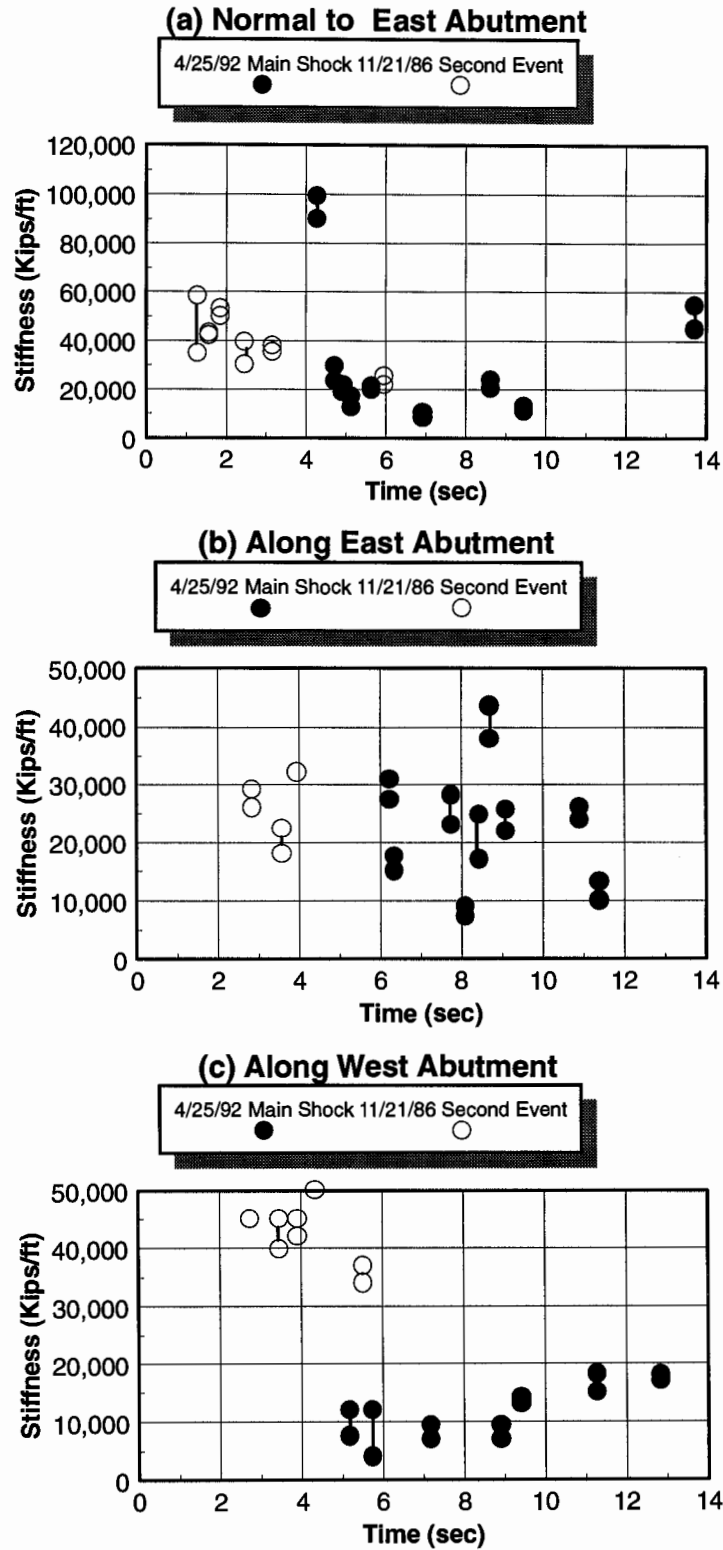*Figure: scatter plot, Stiffness (Kips/ft) vs Time (sec)*

Figure 10. Time-variation of abutment stiffness for two earthquakes

18

TORSIONAL MOTIONS OF THE ROAD DECK

The road deck of the US 101/Painter Street Overpass experienced significant torsional motions (or rotation) about its vertical axis during the main shock of the 1992 Cape Mendocino/Petrolia earthquake; the peak acceleration at the west end of the road deck was more than one-and-a-half times that at the east end during this earthquake (Figure 2). In order to investigate the cause of this behavior of the road deck, the transverse stiffnesses of the east and the west abutments are compared in Figure 11. The transverse stiffness of the west abutment is significantly smaller compared to the east abutment because of several reasons. The two abutments have the same plan dimensions but the west abutment is taller and hence less stiff. Furthermore, the east abutment is constructed monolithic with the footing while the west abutment is seated on a neoprene bearing to permit thermal movement that introduces additional flexibility at the west abutment. The center of rigidity of the deck would be closer to the stiffer of the two abutments, the east abutment, whereas the center of mass would be located close to midway between the two abutments. The resulting eccentricity between the centers of mass and rigidity contributed to the torsional motion of the deck. As shown earlier (Goel and Chopra, 1990), the motion should be larger on the flexible side, the west abutment, and this is consistent with the recorded motions shown in Figure 2.
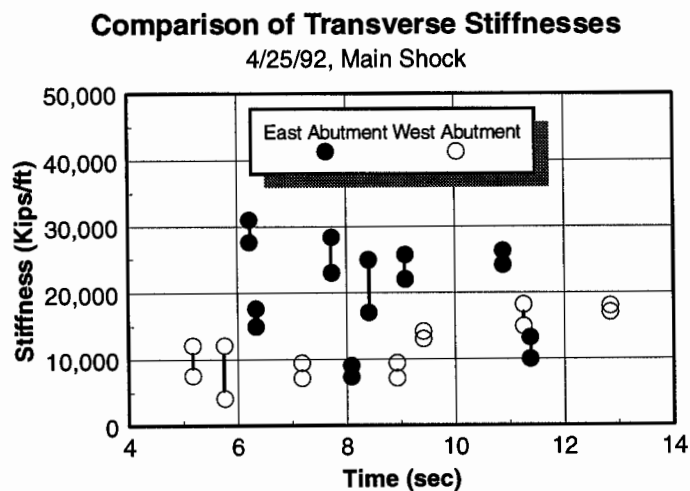

Figure 11. Comparison of transverse stiffnesses of the east and west abutments

EVALUATION OF CURRENT PROCEDURES

Figure 12 compares the abutment stiffness values estimated from recorded motions (Figure 9) with the values computed by the CALTRANS, AASHTO-83, and ATC-6 procedures; the AASHTO-83 and ATC-6 values are identical. Also included are values determined by Gates and Smith (1982) and Romstad and Maroney (1990). The results presented are for the main shock of the 1992 Cape Mendocino/Petrolia earthquake.

In the CALTRANS procedure the stiffness values are determined from the abutment capacity in conjunction with the acceptable deformation (CALTRANS, 1988). Two values of the acceptable deformation are considered: 1 inch and 2.4 inch; the former corresponds to the limit when the soil resistance reaches its maximum value of 7.7 ksf (CALTRANS, 1988), and the latter corresponds to the limiting value for avoiding damage to the abutment (CALTRANS, 1989). The iterative procedure in which the initial stiffness is computed by assuming the soil stiffness of 200 kips/in per linear foot of the abutment backwall or wingwall (Tsai et al., 1993; CALTRANS, 1989) is not included in this investigation because CALTRANS engineers no longer use this procedure. The abutment stiffnesses computed according to the procedure in Memo 5-1 of CALTRANS (1988) are presented in Table 2. The AASHTO-83/ATC-6 values are computed by using the procedure proposed by Lam and Martin (1986) in their report to the Federal Highway Administration; this report supplements the AASHTO-83 document. The detailed calculations for abutment stiffness by these procedures are included in Appendix F.

Figure 12a compares the stiffness normal to the east abutment estimated from the recorded motion (Figure 9a) with the values computed according to the CALTRANS procedure. For each deformation level, the CALTRANS results are shown for four possible failure mode of the abutments; note that the figure shows only three lines because the stiffnesses for two of the four failure modes are almost identical (Table 2). These results show that the stiffness normal to the east abutment during the strong shaking phase matches well with the CALTRANS values for 2.4 inch deformation but tends to be much smaller than the CALTRANS value for one inch deformation. Note that the peak deformation, either in the positive or the negative direction,

20

normal to the east abutment is approximately one inch (Figure 6a). Thus, the CALTRANS procedure using one inch deformation overestimates the stiffness normal to the abutment. During the build-up phase and towards the end of the earthquake, the stiffness values are higher compared to the CALTRANS values for both deformation levels because of much smaller abutment deformation during these phases.

Since the stiffness computed by the AASHTO-83/ATC-6 procedure is an initial estimate, it is larger than the values during the earthquake; it is expected that the final value obtained by the iterative procedure would be closer to the values during the earthquake. The stiffness determined by Gates and Smith is especially large because this value is determined for very low deformations associated with ambient vibration. Since Romstad and Maroney suggested that the abutment is rigid (infinitely stiff) in the longitudinal direction, their value is not included.

Results for the transverse stiffness show that the east abutment is much stiffer during the earthquake compared to the CALTRANS values for both deformation levels -- 1 inch and 2.4 inch -- and the AASHTO-83/ATC-6 value (Figure 12b). This difference can be explained by noting that the earthquake-induced deformations are significantly smaller compared to those assumed in calculating the CALTRANS values; force-deformation loops for this abutment shown in Figure 6b indicate that the abutment deformations during the earthquake are smaller than one-half of an inch. The stiffness tends to be close to the value determined by Gates and Smith from low-level vibration but smaller than the value suggested by Romstad and Maroney based on earthquakes smaller than the 1992 earthquake.

For the west abutment, the CALTRANS values for the two deformation levels form the upper and lower bounds of its stiffness during strong shaking phase (Figure 12c). Since the deformations of this abutment during the strong shaking phase of the earthquake are in the range of values (Figure 6c) assumed in computing the stiffness according to the CALTRANS procedure, this comparison indicates that the CALTRANS procedure leads to a good estimate of the abutment stiffness in the transverse direction. During the less intense motions near the end of the shaking, however, the stiffness values during the earthquake may be higher than both the

CALTRANS values because of much smaller deformation of the abutment. Since the values determined by Gates and Smith (1982) and Romstad and Maroney (1990) are both for smaller deformation levels, these values tend to be much higher than the values during the earthquake. The AASHTO-83/ATC-6 value also tends to be higher than the stiffness value during the earthquake.

Table 2. Abutment stiffness from the CALTRANS procedure

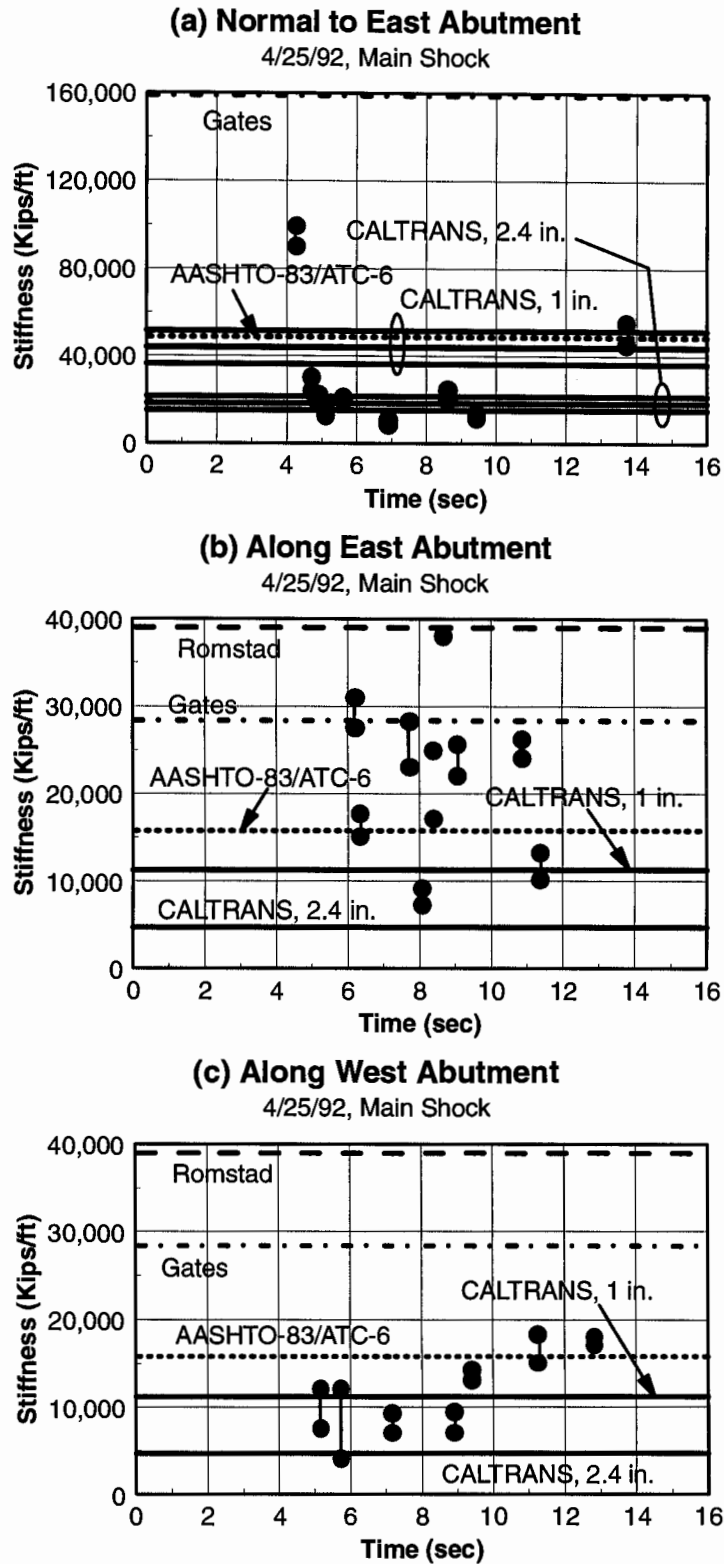| Direction	Stiffness (kips/ft)	Assumptions
Longitudinal	43,960	$EQ_L = R_{SOIL} + V_{DIAPHRAGM}$, Deformation $\leq$ 1 inch.
	36,188	$EQ_L = R_{SOIL} + R_{PILES,\ ONE\ ABUT.}$, Deformation $\leq$ 1 inch.
	51,640	$EQ_L = R_{SOIL} + V_{DIAPHRAGM} + R_{PILES,\ ONE\ ABUT.}$, Deformation $\leq$ 1 inch.
	43,868	$EQ_L = R_{SOIL} + R_{PILES,\ BOTH\ ABUT.}$, Deformation $\leq$ 1 inch.
	18,317	$EQ_L = R_{SOIL} + V_{DIAPHRAGM}$, Deformation = 2.4 inch.
	15,078	$EQ_L = R_{SOIL} + R_{PILES,\ ONE\ ABUT.}$, Deformation = 2.4 inch.
	21,517	$EQ_L = R_{SOIL} + V_{DIAPHRAGM} + R_{PILES,\ ONE\ ABUT.}$, Deformation = 2.4 inch.
	18,278	$EQ_L = R_{SOIL} + R_{PILES,\ BOTH\ ABUT.}$, Deformation = 2.4 inch.
Transverse East	11,187	$EQ_T = V_{WW} + R_{PILES}$, Deformation $\leq$ 1 inch.
	4,661	$EQ_T = V_{WW} + R_{PILES}$, Deformation = 2.4 inch.
Transverse West	10,553	$EQ_T = V_{WW} + 0.75\,R_{PILES}$, Deformation $\leq$ 1 inch.
	4,397	$EQ_T = V_{WW} + 0.75\,R_{PILES}$, Deformation = 2.4 inch.

(a) Normal to East Abutment
4/25/92, Main Shock

Gates

CALTRANS, 2.4 in.

AASHTO-83/ATC-6

CALTRANS, 1 in.

(b) Along East Abutment
4/25/92, Main Shock

Romstad

Gates

AASHTO-83/ATC-6

CALTRANS, 1 in.

CALTRANS, 2.4 in.

(c) Along West Abutment
4/25/92, Main Shock

Romstad

Gates

CALTRANS, 1 in.

AASHTO-83/ATC-6

CALTRANS, 2.4 in.

Figure 12. Comparison of abutment stiffness values determined from recorded motions with the values from current procedures

24

CONCLUSIONS AND RECOMMENDATIONS

In this investigation, abutment stiffnesses are determined directly from the recorded earthquake motions of the US 101/Painter Street Overpass using a simple equilibrium-based approach without finite-element modeling of the structure or of the abutment-soil systems. The values determined in this manner, which include the effects of soil-structure interaction and of nonlinear behavior of the soil, lead to the following conclusions. The abutment stiffness may be significantly different during different phases of the shaking and decreases significantly as the abutment deformation increases. The road deck of this structure experienced significant torsional motions in part because of the differences in transverse stiffnesses of the two abutments. Evaluation of the current modeling procedures for abutment stiffness indicates that the CALTRANS procedure leads to a good estimate of the abutment stiffness in the transverse direction provided the deformation assumed in computing the stiffness is close to the actual deformation during an earthquake, but it appears to overestimate the stiffness in the longitudinal direction. The AASHTO-83 and ATC-6 procedures give initial estimates of abutment stiffnesses in the transverse as well as longitudinal directions which are much higher than the stiffness values during the earthquake.

The approach developed in this investigation provides the most direct means for estimating the abutment stiffness in short bridges during earthquakes and for evaluating the current modeling procedures for abutment-soil systems. Therefore, additional short bridges should be instrumented and their response investigated by this approach. Since recorded earthquake motions are already available for the Meloland Road Overcrossing in El Centro, it would be desirable to study the response of this structure to increase the meager data base on abutment stiffness during earthquake motions and to further evaluate the current modeling procedures.

More accurate values for the abutment stiffness would be obtained if the free-field or input motion at various locations -- abutments and column-bent -- of the structure were available; such data would lead to more reliable estimates of deformation of these components. Therefore additional accelerometers should be deployed at ground level close to the abutment and the

column-bent of the US 101/Painter Street Overpass, the Meloland Road Overcrossing, and other similar structures.

REFERENCES

AASHTO-83. (1988). *Guide Specifications for Seismic Design of Highway Bridges,* American Association of State Highway and Transportation Officials, Washington, D.C.

ATC-6. (1981). *Seismic Design Guidelines for Highway Bridges*, Applied Technology Council, Berkeley, CA, October.

CALTRANS. (1989). *Bridge Design Aids 14-1*, California Department of Transportation, Sacramento, CA, October.

CALTRANS. (1988). *Memo to Designers 5-1,* California Department of Transportation, Division of Structures, Sacramento, CA, September.

Crouse, C. B., Hushmand, B., and Martin, G. R. (1987). "Dynamic Soil-Structure Interaction of A Single-Span Bridge," *Earthquake Engineering and Structural Dynamic*, Vol. 15, pp. 711-729.

Douglas, B. M., Maragakis, E. A., Vrontino, S., and Douglas, B. J. (1990). "Analytical Studies of the Static and Dynamic Response of the Meloland Road Overcrossing," *Proceedings of Fourth U.S. National Conference on Earthquake Engineering,* Vol. 1, pp. 987-996, Palm Springs, California, May 20-24.

Gates, J. H. and Smith, M. J. (1982). *Verification of Dynamic Modeling Method by Prototype Excitation,* FHWA/CA/SD-82/07, California Department of Transportation, Office of Structures Design, Sacramento, California, November.

Goel, R. K. and Chopra, A. K. (1990). *Inelastic Seismic Response of One-Story, Asymmetric-Plan Systems,* Report No. UCB/EERC-90/14, Earthquake Engineering Research Center, University of California, Berkeley, California, October.

Lam, I. P. and Martin, G. R. (1986). *Seismic Design of Highway Bridge Foundations Volume II: Design Procedures and Guidelines*, Report No. FHWA/RD-86/102, Earth Technology Corporation, Long Beach, CA, June.

Levine, M. B., and Scott, R. F. (1989). "Dynamic Response Verification of Simplified Bridge-Foundation Model," *Journal of Geotechnical Engineering,* ASCE, Vol. 115, No. 2, pp. 246-260, February.

Romstad, K. and Maroney, B. (1990). *Interpretation of Painter Street Overcrossing Records to Define Input Motions to the Bridge Superstructure*, Final Report to Department of Conservation, Division of Mines and Geology, Office of Strong Motion Studies, October.

Shakal, A. F., et al. (1992). *CSMIP Strong-Motion Records from the Petrolia, California Earthquakes of April 25-26, 1992*, Report No. OSMS 92-05, California Department of Conservation, Division of Mines and Geology, Office of Strong Motion Studies, May 20.

Sweet, J. and Morrill, K. B. (1993). "Nonlinear Soil-Structure Interaction Simulation of the Painter Street Overcrossing," *Proceedings of the Second Annual Caltrans Seismic research Workshop*, Sacramento, CA, March 16-18.

Tsai, N. C. et al. (1993). *Application of CALTRANS' Current Seismic Evaluation Procedures to Selected Short Bridge Overcrossing Structures,* Technical Report, Dames and Moore, Oakland, CA, June.

Wilson, J. C. (1988). "Stiffness of Non-Skew Monolithic Bridge Abutments for Seismic Analysis," *Earthquake Engineering and Structural Dynamics,* Vol. 14, pp. 339-354.

APPENDIX A: INSTRUMENTATION

The locations of the accelerometers in the plan of the US 101/Painter Street Overpass are shown in Figure 1. The instrumentation consists of a set of triaxial accelerometers located about 320 feet north of the east abutment recording three components of the free-field motion (channels 12, 13, and 14). Triaxial accelerometers also record the three components of the abutment motion adjacent to the road deck: channels 15, 16, and 17 at the east end and channels 18, 19, and 20 at the west end. The instrumentation on the structure consists of three uniaxial accelerometers recording three components of motion at the base of the north column in the two-column bent (channels 1, 2, and 3); two uniaxial accelerometers recording transverse motion of the deck near the west abutment (channel 4) and near the north column face (channel 7); three uniaxial accelerometers recording the vertical motion of the deck near the west abutment (channel 5), approximately mid-way between the west abutment and the central bent (channel 6), and approximately mid-way between the central bent and the east abutment (channel 8); and a set of triaxial accelerometers recording three components of the deck motion near the east abutment (channels 9, 10, and 11). The data from these channels is recorded by two time synchronized recorders housed in an Armco type shelter located near the east abutment. The location coordinates of the four data channels on the structure -- 4, 7, 9, and 11 -- that are used in this investigation are shown in Figure A-1.
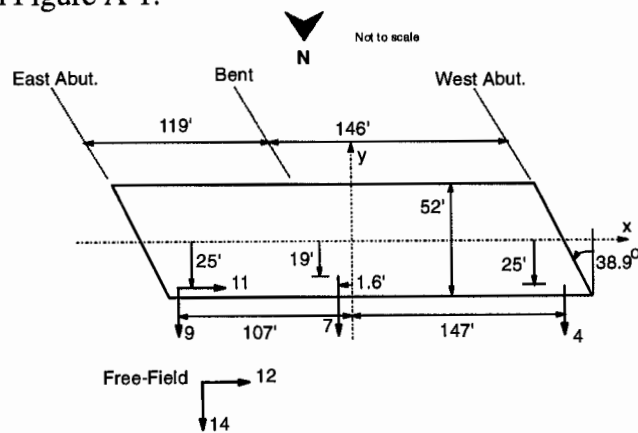
Figure A-1. Location coordinates of data channels

APPENDIX B: COMPUTATION OF ACCELERATIONS AND DISPLACEMENTS

This appendix describes the procedure for computing the two orthogonal components of displacement at any point on the road deck from the displacements at locations of data channels 4, 7, and 9 in the Y-direction and channel 11 in the X-direction; the accelerations can be computed similarly. If the road deck was rigid in its own plane, the horizontal motion at any point on the road deck can be defined in terms of three components of motion at the center of mass (CM) of the road deck: two translational motions in the X- and Y- directions and one rotational motion about the vertical axis (Figure B-1); these three components can be determined from three data channels -- 4 and 9 in the Y-direction and 11 in the X-direction -- through the rigid-body transformation as follows:

$$\begin{Bmatrix} u_x \\ u_y \\ u_\theta \end{Bmatrix} = \begin{bmatrix} \dfrac{25}{254} & -\dfrac{25}{254} & 1 \\ -\dfrac{107}{254} & -\dfrac{147}{254} & 0 \\ -\dfrac{1}{254} & \dfrac{1}{254} & 0 \end{bmatrix} \begin{Bmatrix} u_4 \\ u_9 \\ u_{11} \end{Bmatrix} \tag{B-1}$$

in which the location of the data channels, shown in Figure A-1, has been utilized.
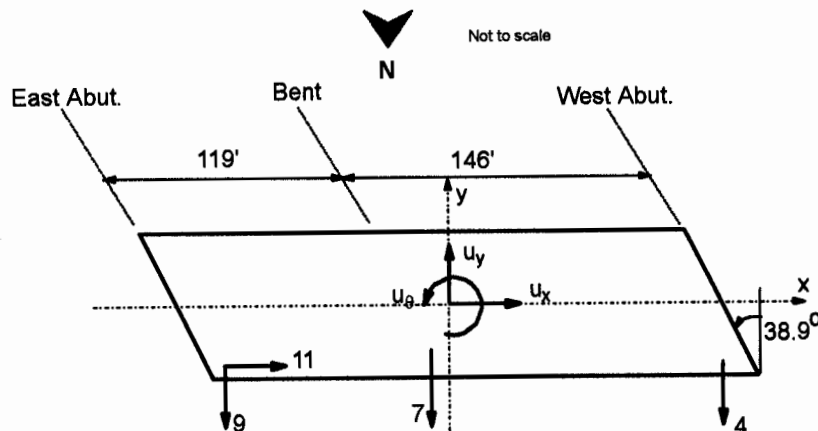
Figure B-1. Degrees of freedom corresponding to the rigid-body motion

The X- and Y-components of the displacements at any location with coordinates x and y due to the rigid-body motion are:

$$\begin{Bmatrix} \hat{v}_x \\ \hat{v}_y \end{Bmatrix} = \begin{bmatrix} 1 & 0 & -y \\ 0 & 1 & x \end{bmatrix} \begin{Bmatrix} u_x \\ u_y \\ u_\theta \end{Bmatrix} \qquad \text{(B-2)}$$

If the road deck were not rigid in its own plane, additional motions due to in-plane deformations would have to be included; since the road deck is rigid in the X-direction, the additional deformations need to be considered only in the Y-direction (transverse direction). The total displacement is equal to the displacement due to rigid-body motion (Equation B-2) and the in-plane deformations in the Y-direction given as:

$$\begin{Bmatrix} v_x \\ v_y \end{Bmatrix} = \begin{Bmatrix} \hat{v}_x \\ \hat{v}_y - \Delta u_y(x) \end{Bmatrix} \qquad \text{(B-3)}$$

in which the in-plane deformation $\Delta u_y(x)$ is computed by fitting a half-sine function with an amplitude equal to the in-plane deformation at the CM of the road deck, Δu_{yo} (Figure B-2); the $\Delta u_y(x)$ is considered to be subtractive in Equation B-3 because the positive direction of the y-axis is opposite to the positive direction of the data channels.

$$\Delta u_y(x) = \Delta u_{yo} \sin\left(\frac{\pi}{2} + \pi \frac{x}{265} \right) \qquad \text{(B-4)}$$
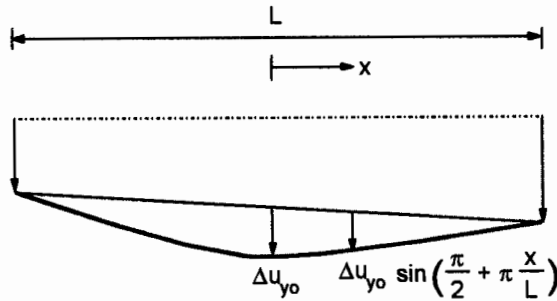
Figure B-2. Computation of in-plane deformation

The approach of fitting half-sine function is based on the simplifying assumption that the road deck can be represented as a simply-supported beam with uniform distribution of mass vibrating in its fundamental mode. Since the abutments (or supports) are skewed, the vibration mode of the

beam is assumed to be along the skew angle. Utilizing this assumption, the Δu_{yo} is computed as follows.

Figure B-3 shows assumed pattern of the road deck along with its deformations at the locations of sensors 4, 7, and 9. The locations of these sensors are determined with respect to the transverse axis along the skew angle and originating at the CM (Figure B-4).
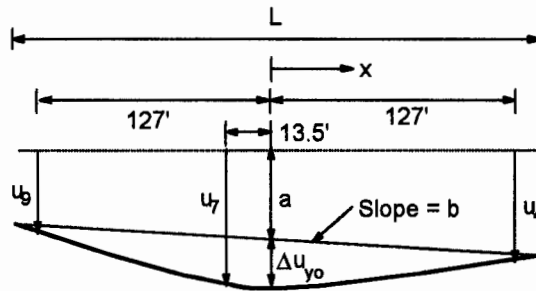

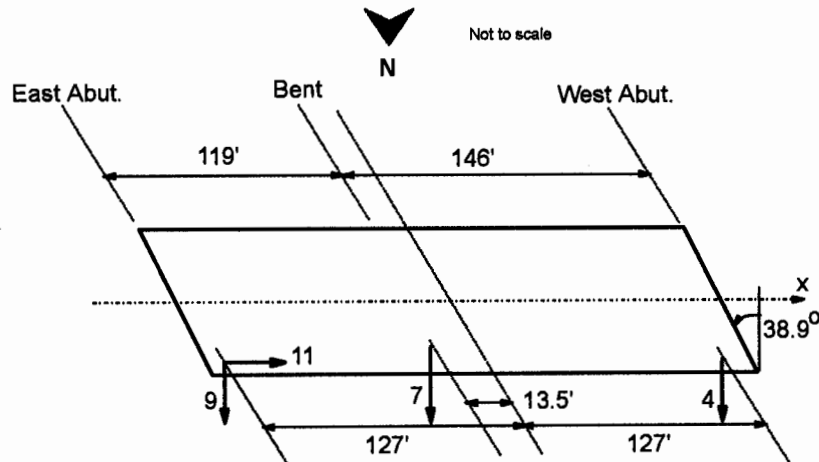Figure B-3. Deformation pattern of the road deck

Figure B-4. Location of the sensors with respect to the skewed transverse axis

Let a be the intercept and b the slope of the rigid-body motion of the road deck (Figure B-3). Then the motions at the location of the three sensors are:

$$u_4 = a + 127b + \Delta u_{yo} \sin\left(\frac{\pi}{2} + \pi\frac{127}{265}\right)$$ (B-5a)

$$u_7 = a - 13.5b + \Delta\, u_{yo} \sin\left(\frac{\pi}{2} - \pi\frac{13.5}{265}\right) \tag{B-5b}$$

$$u_9 = a - 127b + \Delta\, u_{yo} \sin\left(\frac{\pi}{2} - \pi\frac{127}{265}\right) \tag{B-5c}$$

Neglecting the last term in Equations B-5a and B-5c, which are expected to be small compared to the sum of the first two terms, and further simplifying Equation B-5b lead to

$$u_4 = a + 127b \tag{B-6a}$$

$$u_7 = a - 13.5b + \Delta\, u_{yo} \sin\left(\frac{119}{265}\pi\right) \tag{B-6b}$$

$$u_9 = a - 127b \tag{B-6c}$$

Solving equations B-6a and B-6c for a and b and utilizing these results in Equation B-6b gives

$$\Delta\, u_{yo} = \frac{1}{\sin\left(\pi\dfrac{119}{265}\right)}\left(u_7 - \frac{113.5}{254}u_4 - \frac{140.5}{254}u_9\right) \tag{B-7}$$

In order to examine whether the road deck behaved as rigid in the transverse direction, plotted in Figures B-5 and B-6 are the deformed shapes, which include effects of both the rigid-body motions and the in-plane deformation, at several time instances during the two selected earthquakes. These Figures show that while the in-plane deformations during the 1992 earthquake are small compared to the rigid-body motions, they are significant during the 1986 earthquake. For the sake of consistency, the in-plane deformations are included for both the earthquakes.

Required in this investigation are the relative displacements in the spring-damper systems representing the abutments and springs representing the columns. These are computed as follows. First, the relative displacements along the global X- and Y-directions are computed by subtracting the free-field displacements from the total displacements (Equation B-3) as:

33

First, the relative displacements along the global X- and Y-directions are computed by subtracting the free-field displacements from the total displacements (Equation B-3) as:

$$\begin{Bmatrix} \tilde{v}_x \\ \tilde{v}_y \end{Bmatrix} = \begin{Bmatrix} v_x - u_{12} \\ v_y - u_{14} \end{Bmatrix} \tag{B-8}$$

Implicit in Equation (B-8) is the assumption that the free-field motion is the input motion which is same at all locations.

The relative displacements at locations of these systems are then computed by applying a rotation transformation to the displacements obtained from Equation (B-8) as:

$$\begin{Bmatrix} v'_x \\ v'_y \end{Bmatrix} = \begin{bmatrix} \cos\theta & \sin\theta \\ -\sin\theta & \cos\theta \end{bmatrix} \begin{Bmatrix} \tilde{v}_x \\ \tilde{v}_y \end{Bmatrix} \tag{B-9}$$

It should be noted that the displacements at the locations of data channels 4, 7, 9, 11, 12, and 14 that are used in the aforementioned procedure are derived by double integrating the corrected accelerations. Both the corrected accelerations and the displacements are provided by the CSMIP.

Between 0 and 2 Seconds

Between 2 and 4 Seconds

Between 4 and 6 Seconds

Between 6 and 8 Seconds

Between 8 and 10 Seconds

Between 5.2 and 5.4 Seconds
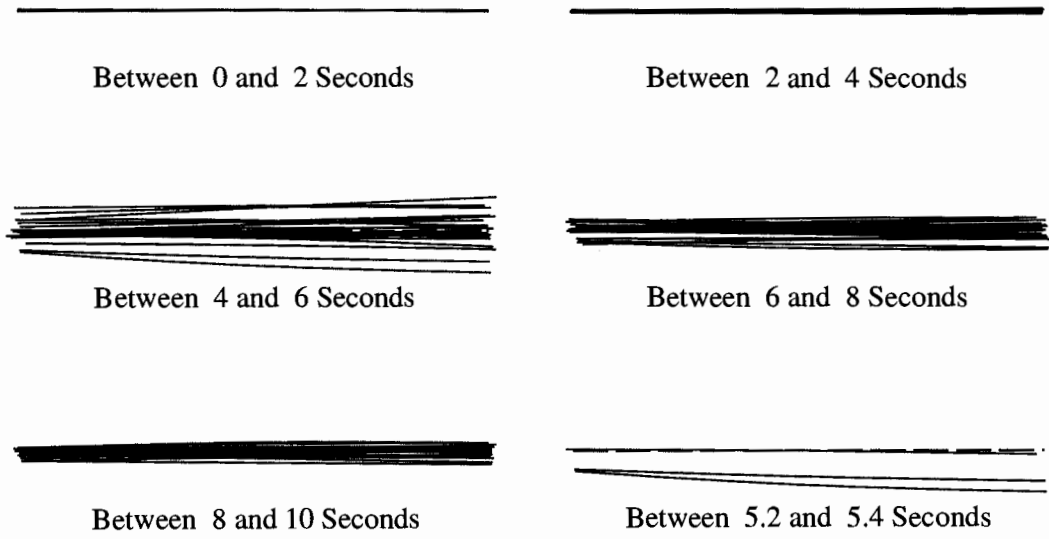
Figure B-5. Displacement history, relative to free-field, for US 101/Painter Street Overpass during the 1992 earthquake

Between 0 and 2 Seconds

Between 2 and 4 Seconds

Between 4 and 6 Seconds

Between 6 and 8 Seconds

Between 8 and 10 Seconds

Between 1 and 2 Seconds
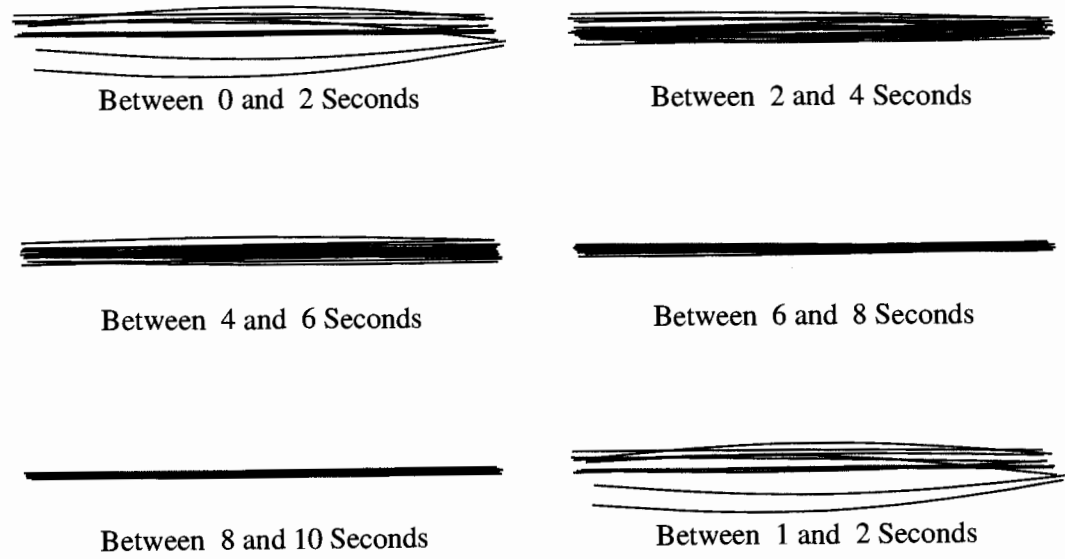
Figure B-6. Displacement history, relative to free-field, for US 101/Painter Street Overpass during the 1986 earthquake

APPENDIX C: COMPUTATION OF INERTIA FORCES

The inertia forces are computed from the mass of the road deck and the recorded accelerations. The total mass of the road deck is based on the unit weight of 14.78 kips/ft suggested by Gates and Smith (1982). The mass per unit area is determined by assuming that the total mass is uniformly distributed over the entire area of the road deck. The three components of the inertia force are computed as:

$$\begin{Bmatrix} f_x \\ f_y \\ f_\theta \end{Bmatrix} = \begin{Bmatrix} f_x^{RB} \\ f_y^{RB} \\ f_\theta^{RB} \end{Bmatrix} + \begin{Bmatrix} 0 \\ \Delta f_y \\ 0 \end{Bmatrix} \tag{C-1}$$

The first term on the right hand side of Equation (C-1) is the contribution due to the rigid-body motion of the road deck and the second term is the contribution due to the in-plane deformation in the Y-direction. The contribution of the rigid-body motions is computed:

$$\begin{Bmatrix} f_x^{RB} \\ f_y^{RB} \\ f_\theta^{RB} \end{Bmatrix} = \begin{bmatrix} m_x & 0 & 0 \\ 0 & m_y & 0 \\ 0 & 0 & I_\theta \end{bmatrix} \begin{Bmatrix} \ddot{u}_x \\ \ddot{u}_y \\ \ddot{u}_\theta \end{Bmatrix} \tag{C-2}$$

in which m_x, m_y, and I_θ are the coefficients of the mass matrix at the center of mass (CM) and $\ddot{u}_x$, $\ddot{u}_y$, and $\ddot{u}_\theta$ are the three components of accelerations at the CM determined from accelerations recorded at channels 4, 9, and 11 using the procedure described in Appendix B. The contribution due to the in-plane deformation of the road deck in the Y-direction is computed as:

$$\Delta f_y = \int_{-L/2}^{L/2} \overline{m} \Delta \ddot{u}_{yo} \sin\left(\frac{\pi}{2} + \frac{\pi x}{L}\right) dx \tag{C-3}$$

in which $\overline{m}$ is the mass per unit length of the road deck and $\Delta \ddot{u}_{yo}$ is the acceleration due to the in-plane deformation of the deck computed by procedure described in Appendix B.

APPENDIX D: COMPUTATION OF FORCES IN COLUMN SPRINGS

The force in each of the four column springs is computed as the product of the column stiffness and the deformation. The deformation, taken as the displacement at the top of the column relative to the free-field, is computed by the procedure described in Appendix B. The stiffness is determined by frame analyses as described next.

Since each column is represented by two springs -- one along the bent and other normal to the bent -- the stiffness of the column is computed in the two directions. For the purpose of computing the stiffness along the bent, the lateral stiffness of the bent frame (Figure D-1) is determined by static condensation of the two rotational degrees of freedom at the two beam-column joints. The total lateral stiffness of the bent frame, thus determined, is divided equally between the two columns. The EI_c for the column is selected as the cracked value in the moment-curvature relationship and the EI_b is computed from the structural details of the cap-beam.
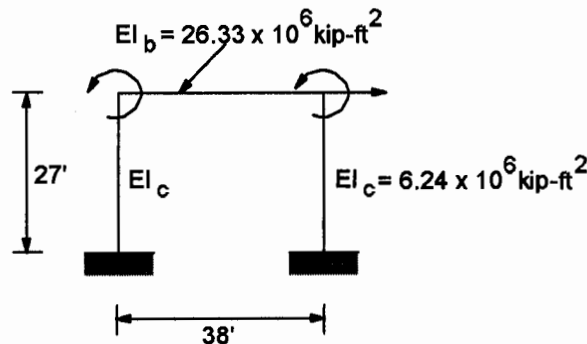
Figure D-1. Frame used for computing the column stiffness along the bent

The stiffness values of the springs normal to the bent are determined by applying the aforementioned procedure on the frame consisting of the columns and the road deck box girder (Figure D-2) with EI_b value in this frame selected as the value for the road deck girder recommended by Gates and Smith (1982). This leads to values of the both the springs, k_4 and k_5 (figure 4), equal to $0.85 \times 12EI_c / h^3$ in which $EI_c = 6.24 \times 10^6$ kip$-$ft^2 and $h = 27$ ft.
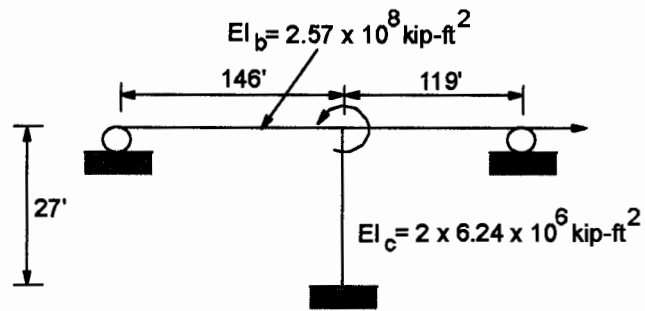
Figure D-2. Frame used for computing the column stiffness normal to the bent

APPENDIX E: DETERMINATION OF ABUTMENT STIFFNESS

Presented in this appendix is the procedure for determining the abutment stiffness followed by the procedure for constructing the figures showing time-variation of the abutment stiffness. As mentioned previously, the abutment stiffness is determined from individual loops that are isolated from the complete force-deformation hysteresis loops. Such individual loops are presented in Figures E-1 to E-3 for the 1992 earthquake and Figures E-4 to E-6 for the 1986 earthquake; for each earthquake, the results are presented for each of the three springs-- normal to the east abutment, along the east abutment, and along the west abutment. These Figures show that while many loops close completely, several others do not. In some cases, it has been possible to identify only the loading or the unloading branch. This occurs because of the earthquake loading, which tends to be very erratic compared to the harmonic loading; the loops for the latter are expected to be closed. Some of the loops are essentially elliptical in shape, whereas others deviate from the elliptical shape considerably. Described next is the procedure for extracting the abutment stiffness from these loops.

For essentially linear viscoelastic behavior of the spring indicated by almost elliptical shape of the loop (Figures E-3g and E-5b), the stiffness is obtained by selecting the slope of the major axis of the ellipse; in general two slopes are selected to obtain the upper and lower bound values. For other loops for which the shape may deviate considerably from a perfect ellipse (Figures E-1b, E-2b, E-2f, E-6a, E-6c, E-6g), it is still possible to obtain the upper and lower bound values of the stiffness in a similar manner. The two bounding values of the stiffness from the loading or unloading branch (Figures E-4c, E-4e, E-5a, E-5d, E-6b, E-6d, and E-6e) are obtained by selecting its slope. For loops that exhibit significant nonlinearity (Figures E-1c, E-1d, E-3a, E-3b), the upper and lower bound values of stiffness are obtained by selecting the secant slopes in the positive and negative directions; the secant slope is defined as the peak force divided by the peak deformation. For loops that do not fit into any of the above mentioned categories, i.e., either the loop does not close or it exhibits some nonlinearity (Figures E-1a, E-1e, E-1f to E-1j, E-2a, E-2c

to E-2e, E-2g to E-2j, E-3c to E-3f, E-4a, E-4d, E-4f, E-5c, E-6a, E-6f, E-6g), the bounding values of the stiffness are determined by a combination of the above described procedures.

Explained next is the procedure for constructing the figures for time-variation of the abutment stiffness (Figure 9 to 12). For this purpose, presented in Figure E-7 is such a time-variation of stiffness along the west abutment during the 1992 earthquake. In this figure, the two bounding values of the stiffness, obtained from the individual hysteresis loop, are plotted as two discrete points, connected by a veryical line, at the time corresponding to the middle of the loop. For example, the two points at 5.19 sec that are identified by label "a" are the upper and lower bound values -- 12000 kips/ft and 7500 kips/ft -- obtained from the hysteresis loop of Figure E-3a. Similarly, the points identified by labels "b" through "g" are obtained from Figure E-3b to E-3g. The time variation of the total deformation (Figure 9) is constructed in a similar manner by plotting a point at a value equal to the total deformation, which is the sum of the deformation amplitudes in the positive and negative directions.
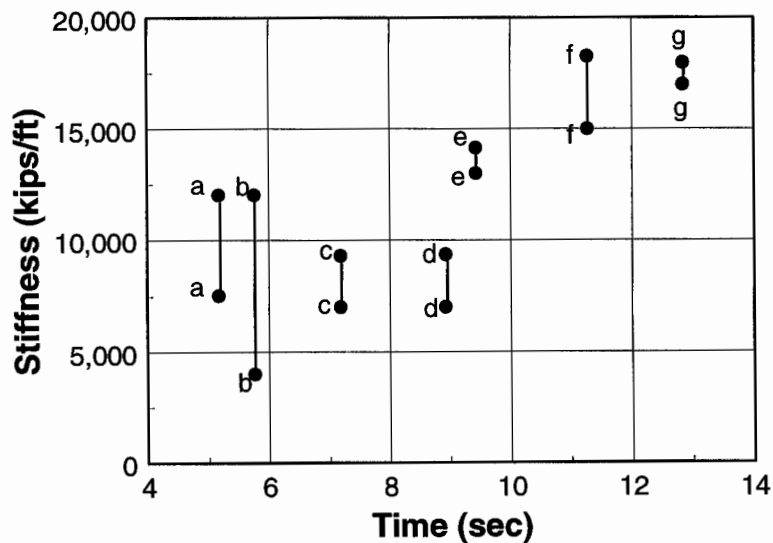
Figure E-7. Construction of time variation of stiffness
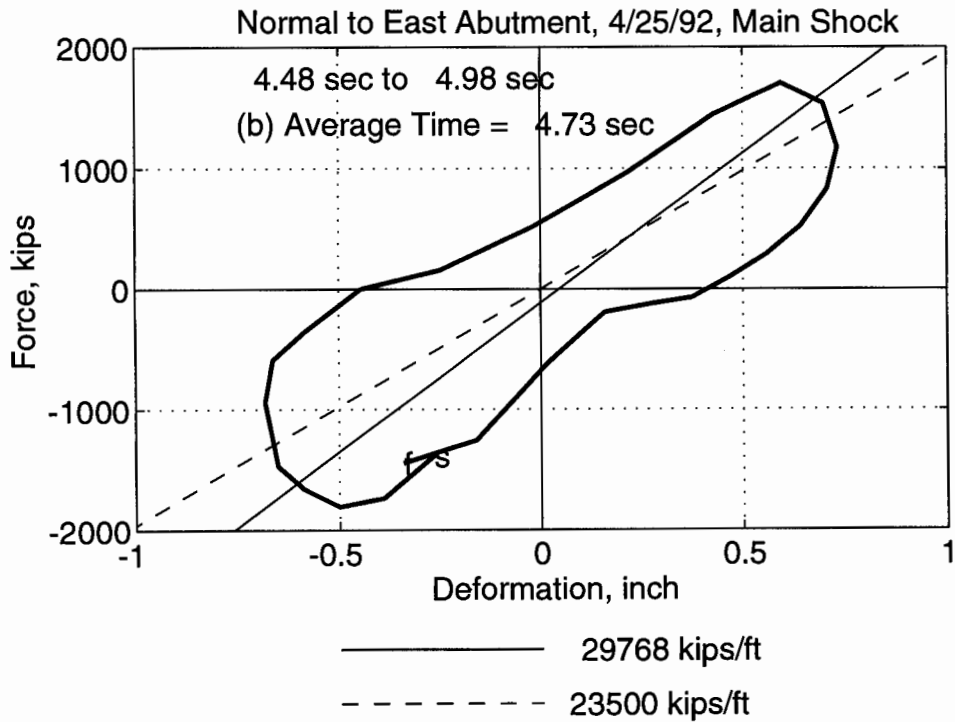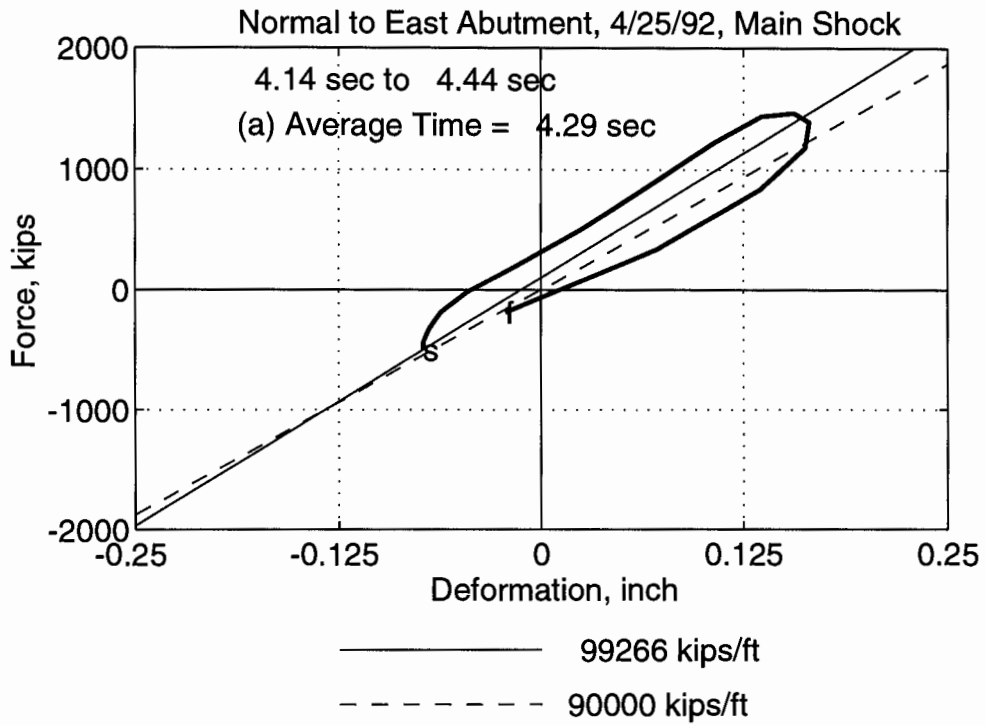
Normal to East Abutment, 4/25/92, Main Shock

4.14 sec to 4.44 sec
(a) Average Time = 4.29 sec

99266 kips/ft
90000 kips/ft

Normal to East Abutment, 4/25/92, Main Shock

4.48 sec to 4.98 sec
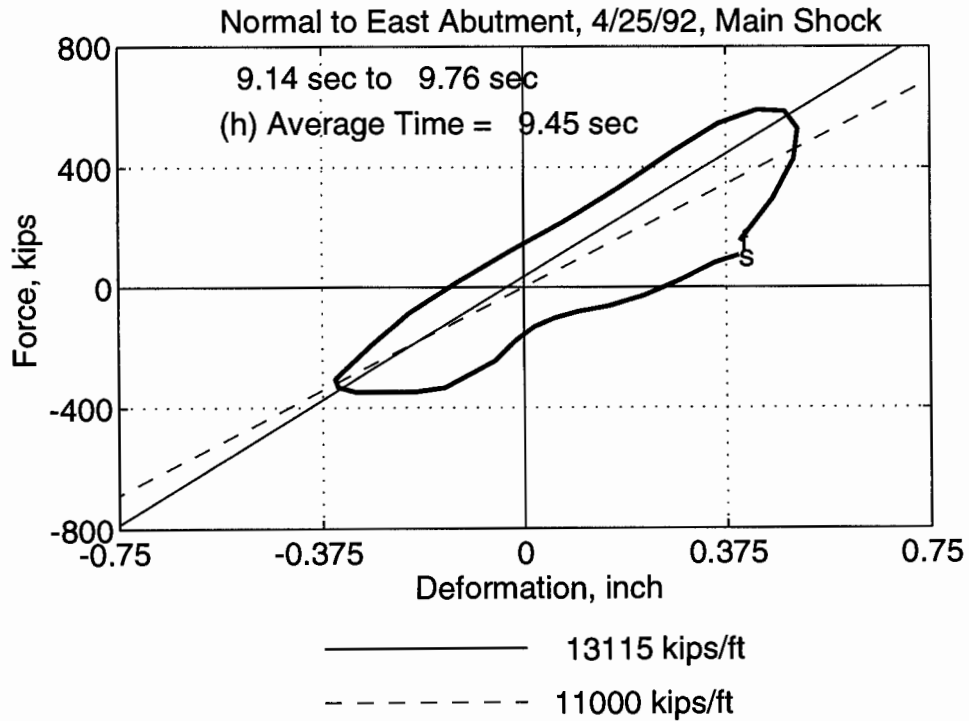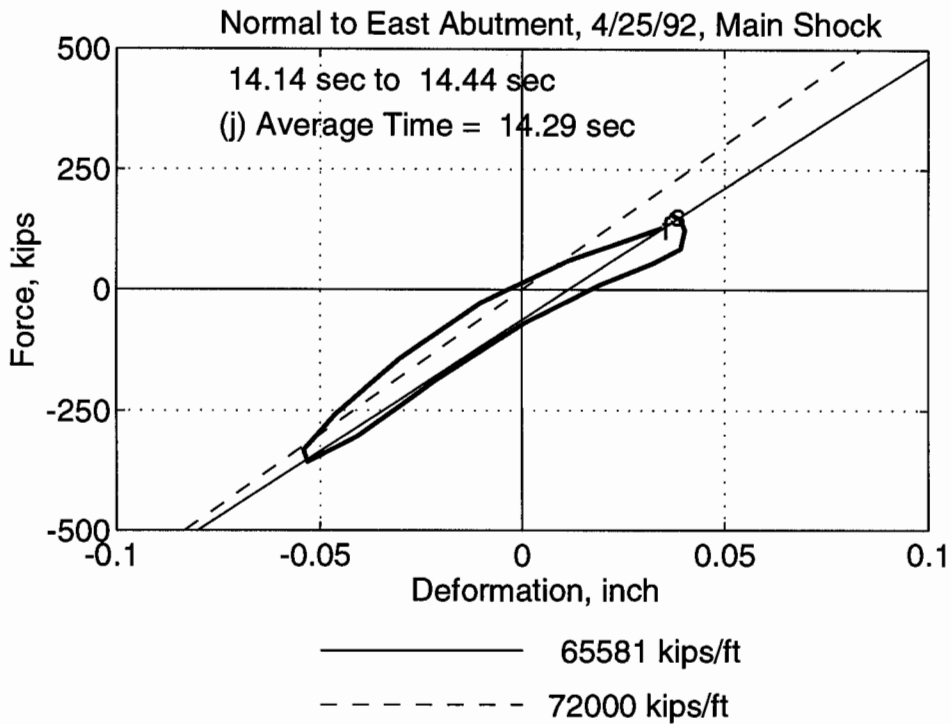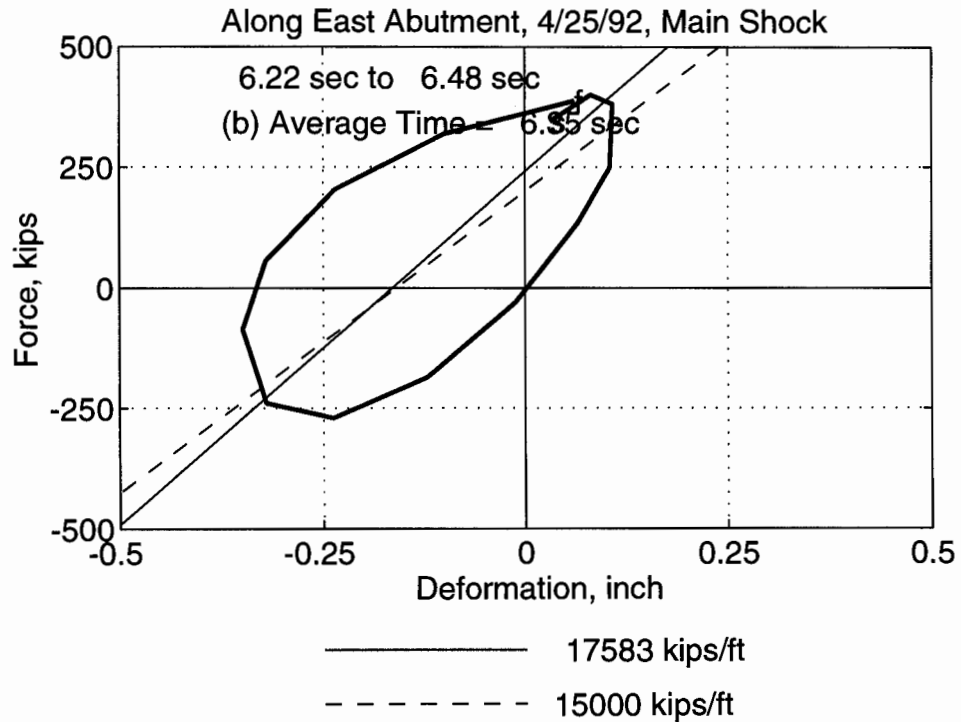(b) Average Time = 4.73 sec

29768 kips/ft
23500 kips/ft

Figure E-1. Individual loops for the spring normal to east abutment during the 1992 earthquake

41

Normal to East Abutment, 4/25/92, Main Shock

4.66 sec to   5.22 sec
(c) Average Time =   4.94 sec

——————— 21691 kips/ft
— — — — — — 18500 kips/ft

Normal to East Abutment, 4/25/92, Main Shock

4.86 sec to   5.40 sec
(d) Average Time =   5.13 sec

——————— 17264 kips/ft
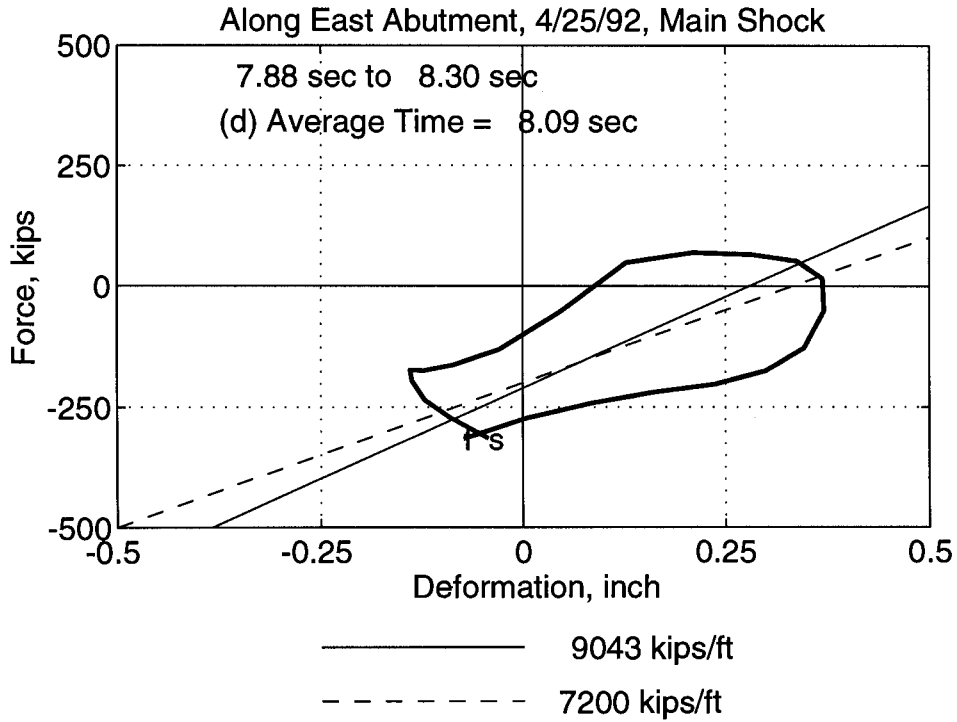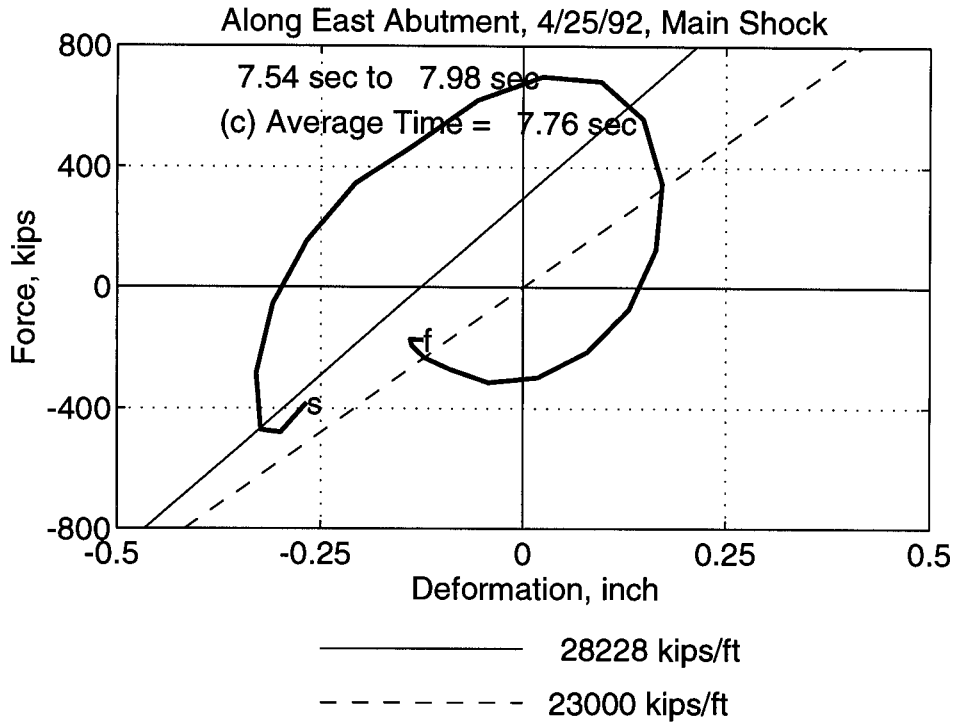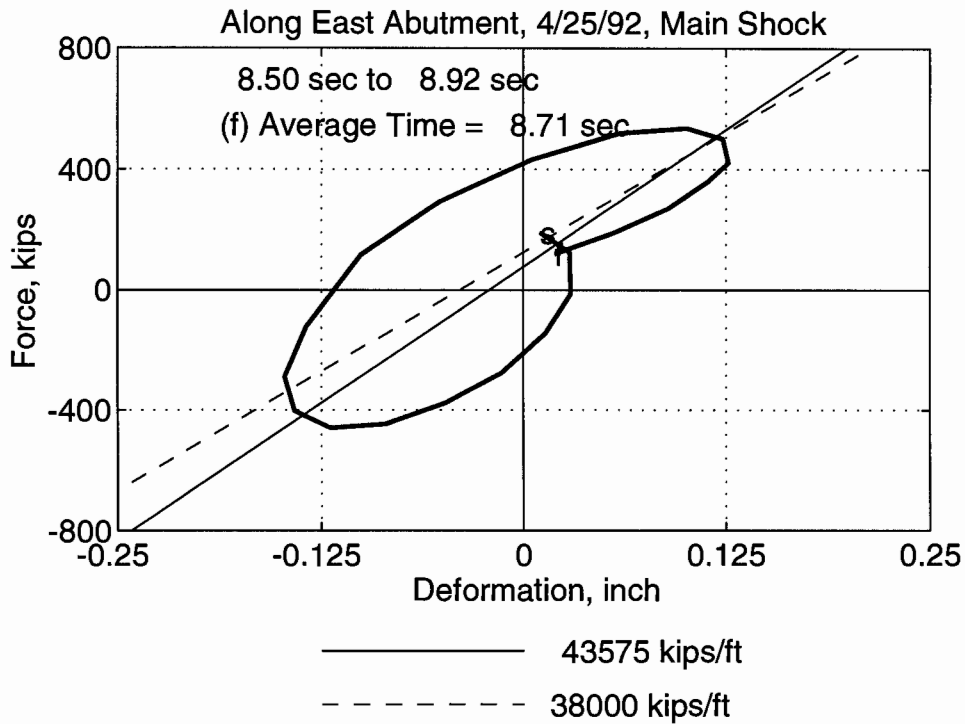— — — — — — 12400 kips/ft

Figure E-1. Individual loops for the spring normal to east abutment during the 1992 earthquake (continued)
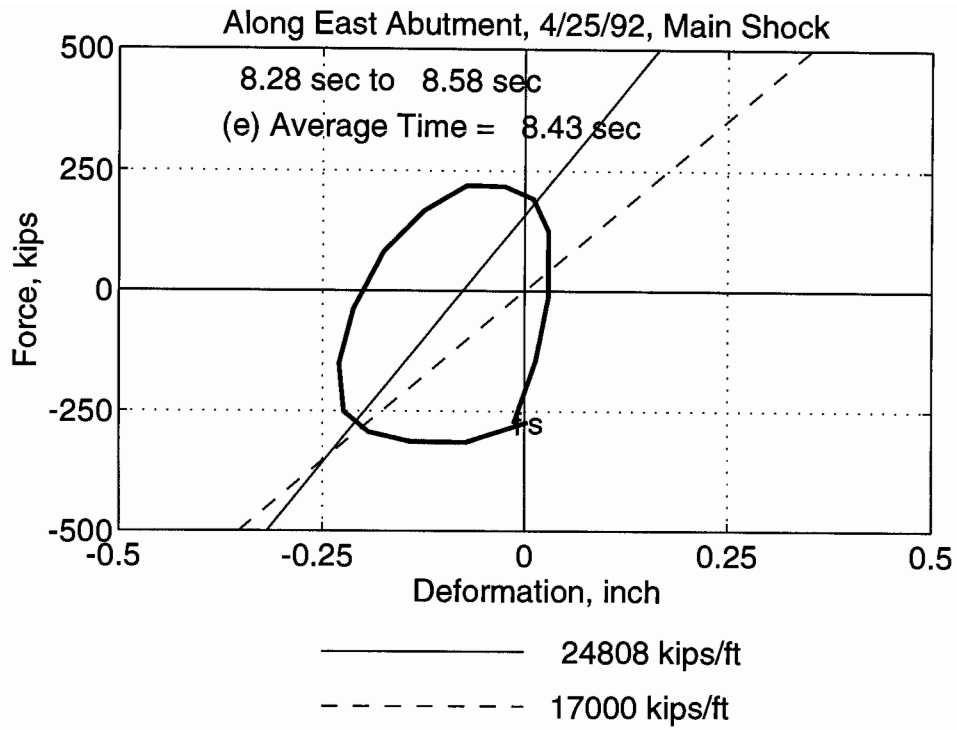
42
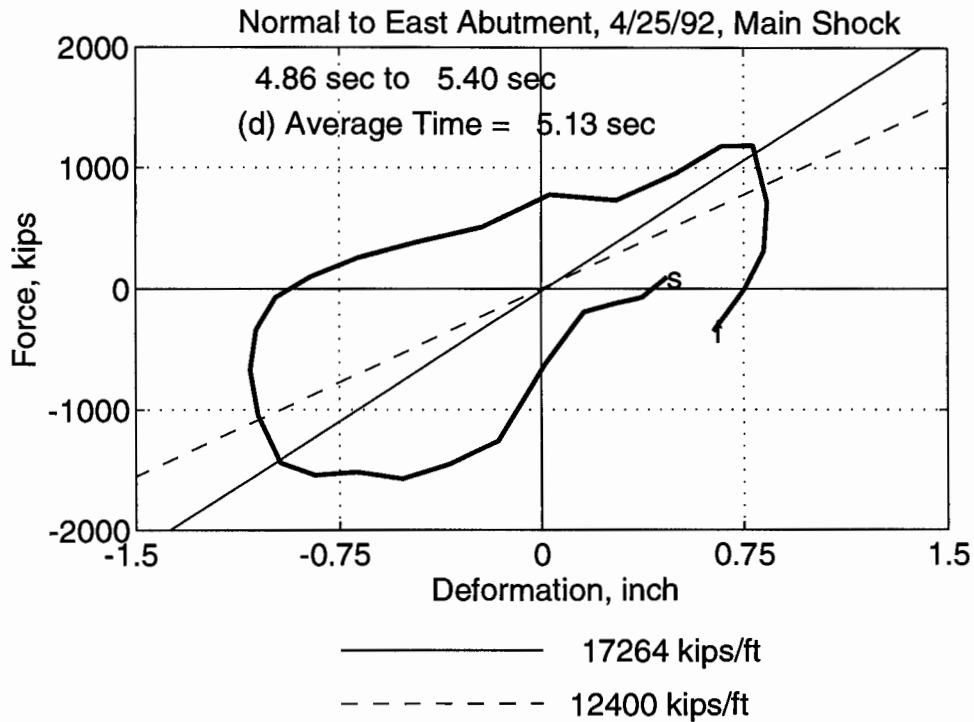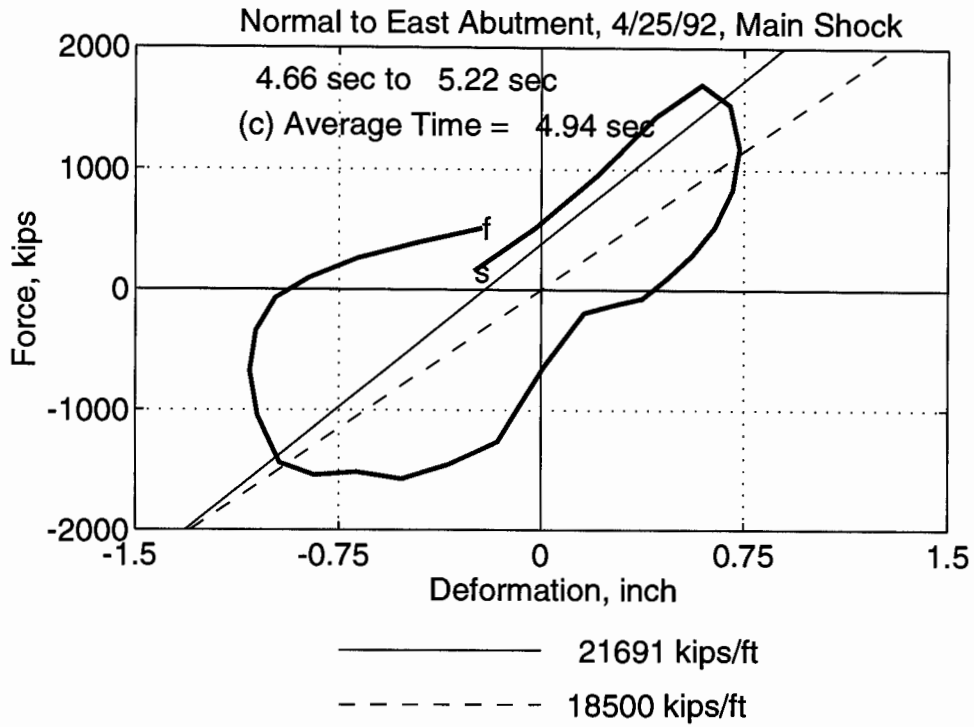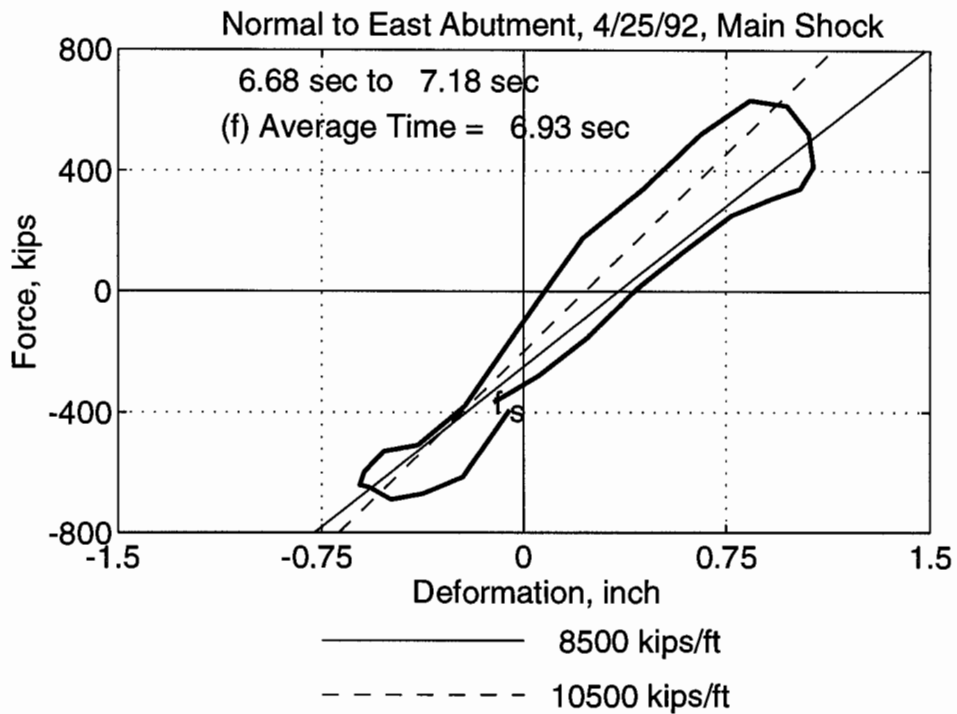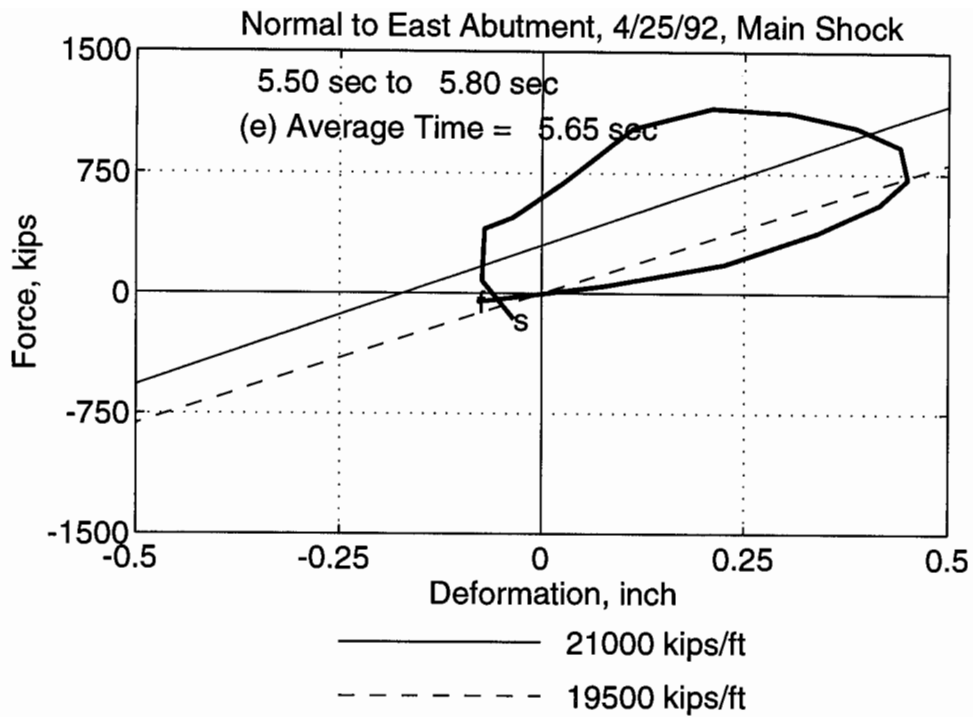
Figure E-1. Individual loops for the spring normal to east abutment during the 1992 earthquake (continued)

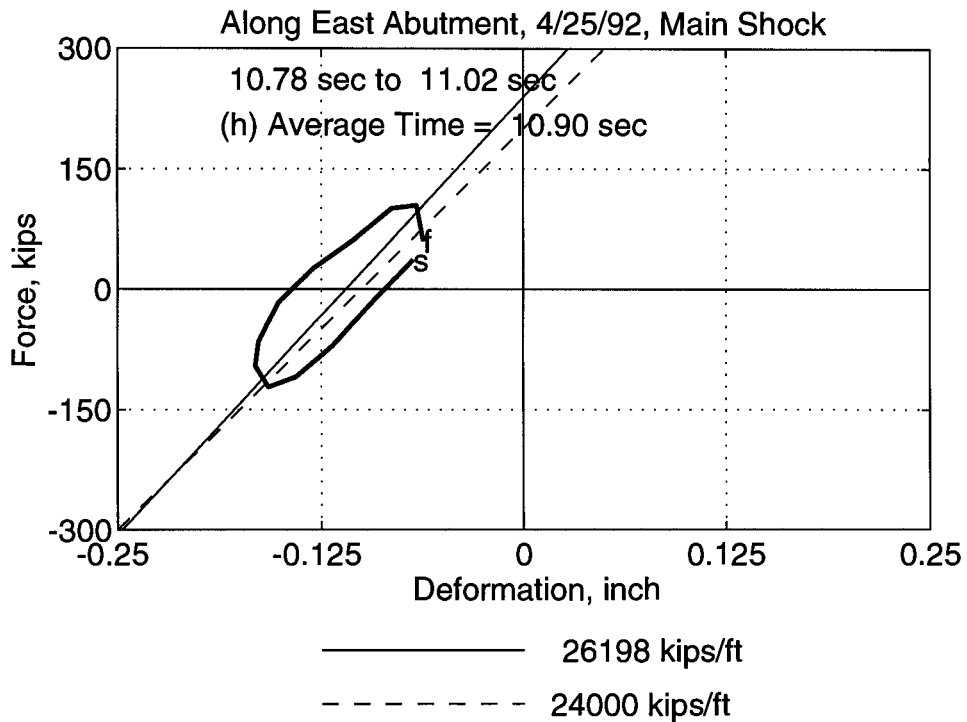Figure E-1. Individual loops for the spring normal to east abutment during the 1992 earthquake (continued)

Normal to East Abutment, 4/25/92, Main Shock

13.50 sec to 13.96 sec
(i) Average Time = 13.73 sec

—————— 54790 kips/ft
– – – – – – 45000 kips/ft

Normal to East Abutment, 4/25/92, Main Shock

14.14 sec to 14.44 sec
(j) Average Time = 14.29 sec

—————— 65581 kips/ft
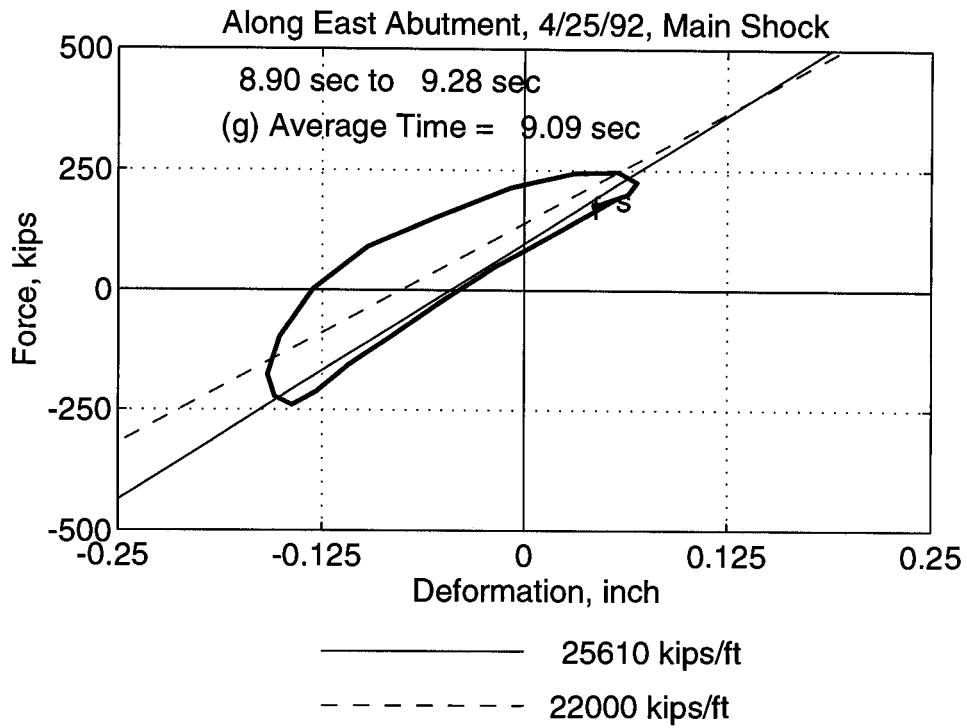– – – – – – 72000 kips/ft

Figure E-1. Individual loops for the spring normal to east abutment during the 1992 earthquake (continued)

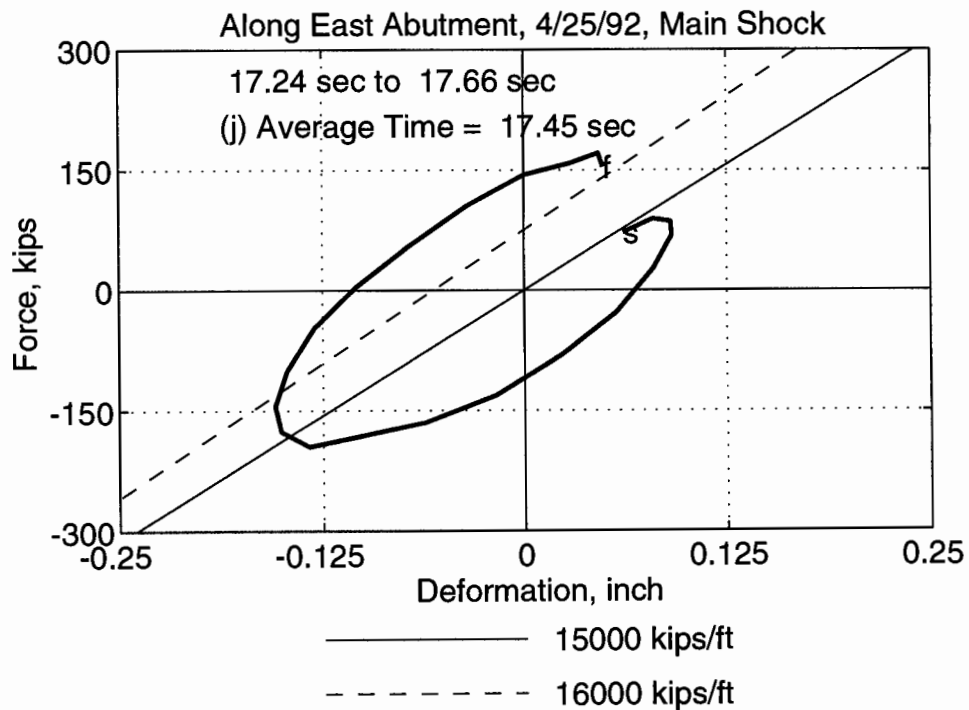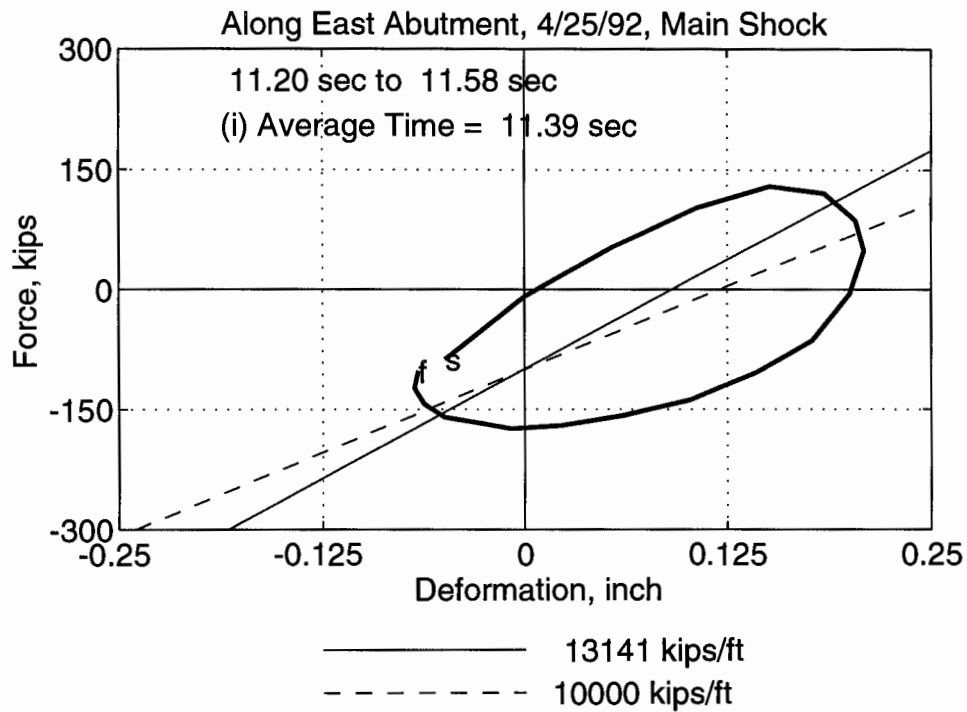Figure E-2. Individual loops for the spring along east abutment during the 1992 earthquake

Along East Abutment, 4/25/92, Main Shock

7.54 sec to   7.98 sec

(c) Average Time =   7.76 sec

28228 kips/ft

23000 kips/ft

Along East Abutment, 4/25/92, Main Shock

7.88 sec to   8.30 sec

(d) Average Time =   8.09 sec

9043 kips/ft

7200 kips/ft

Figure E-2. Individual loops for the spring along east abutment during the 1992 earthquake (continued)

47

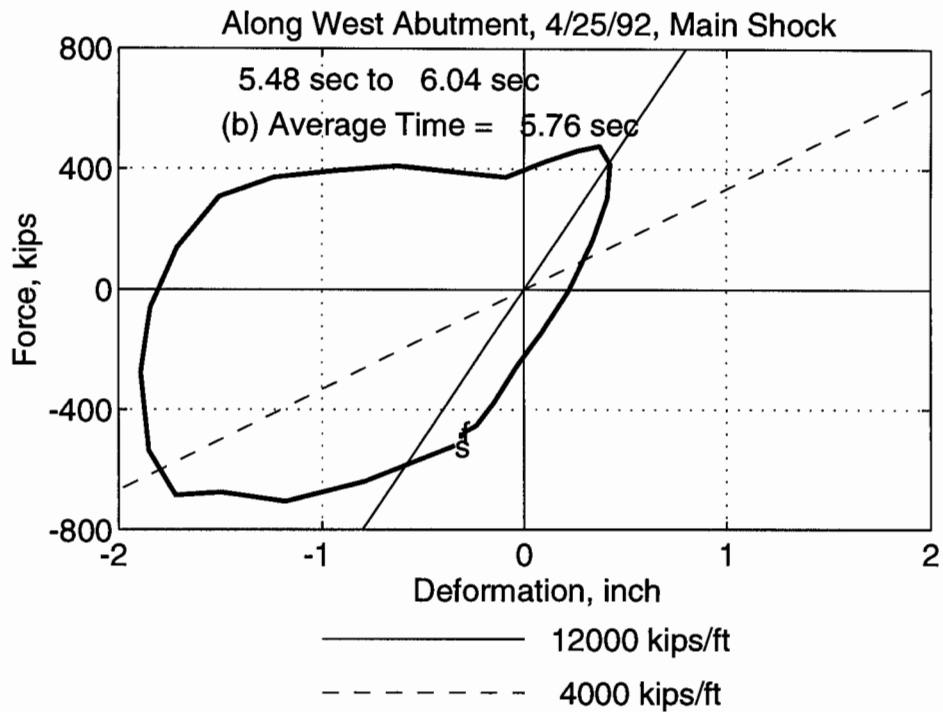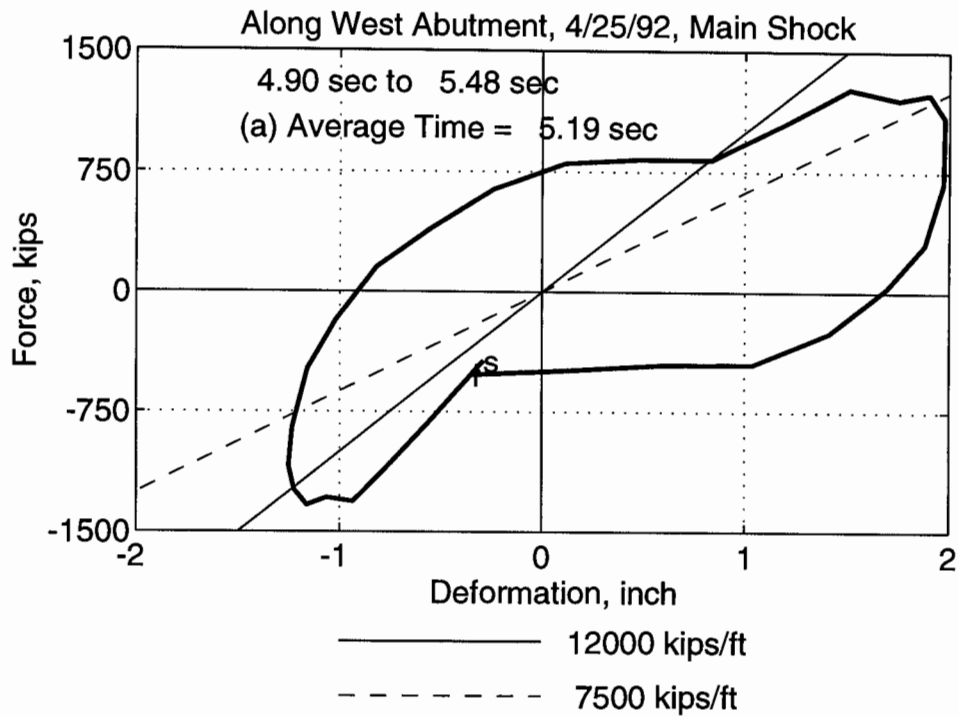Figure E-2. Individual loops for the spring along east abutment during the 1992 earthquake (continued)

Along East Abutment, 4/25/92, Main Shock

8.90 sec to 9.28 sec

(g) Average Time = 9.09 sec

—————— 25610 kips/ft

— — — — — 22000 kips/ft

Along East Abutment, 4/25/92, Main Shock

10.78 sec to 11.02 sec

(h) Average Time = 10.90 sec

—————— 26198 kips/ft

— — — — — 24000 kips/ft

Figure E-2. Individual loops for the spring along east abutment during the 1992 earthquake (continued)

Figure E-2. Individual loops for the spring along east abutment during the 1992 earthquake (continued)
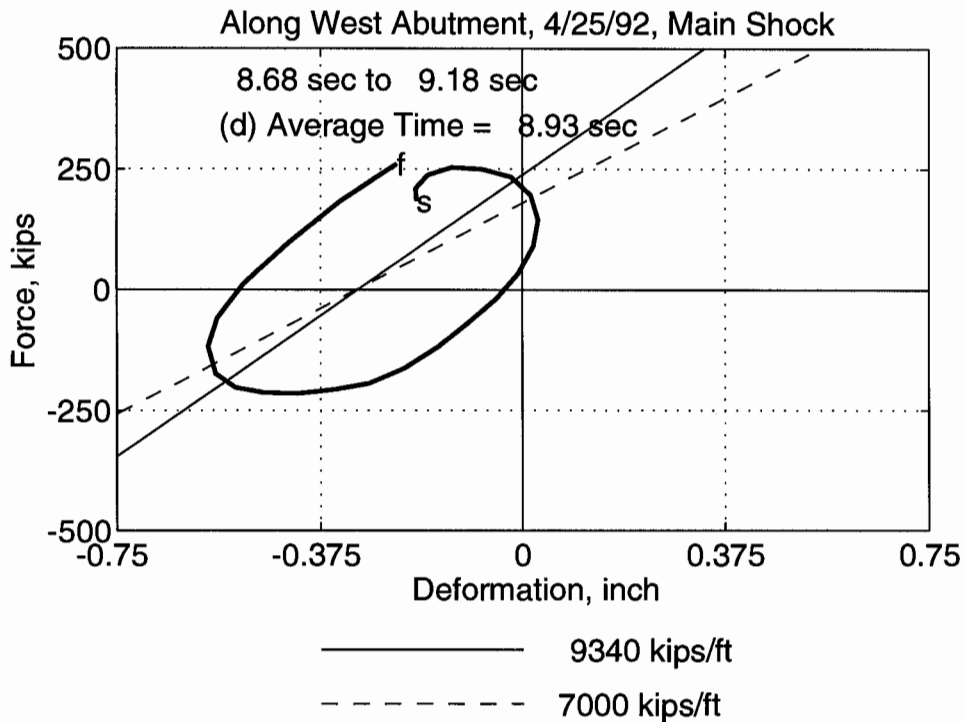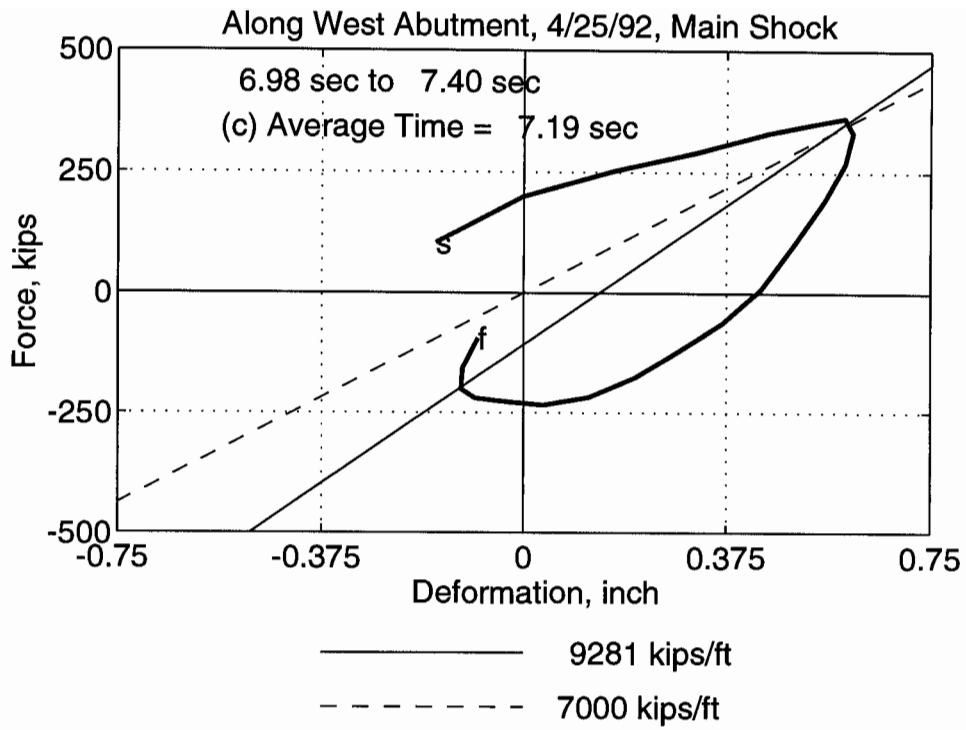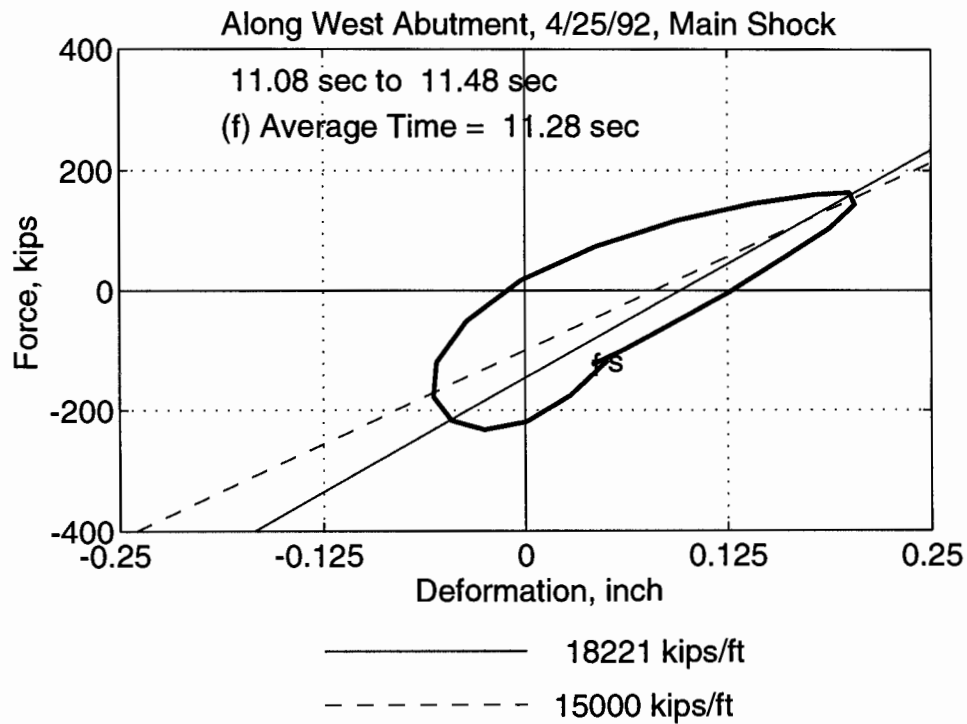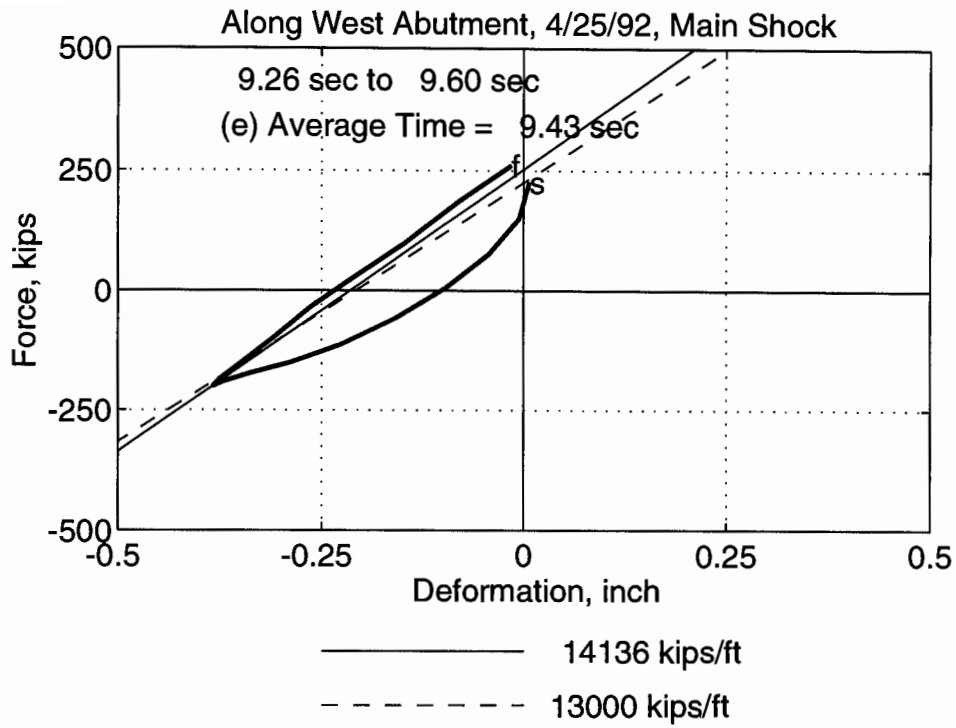
Along West Abutment, 4/25/92, Main Shock

4.90 sec to 5.48 sec
(a) Average Time = 5.19 sec

— 12000 kips/ft
-- 7500 kips/ft

Along West Abutment, 4/25/92, Main Shock

5.48 sec to 6.04 sec
(b) Average Time = 5.76 sec

— 12000 kips/ft
-- 4000 kips/ft

Figure E-3. Individual loops for the spring along west abutment during the 1992 earthquake

Along West Abutment, 4/25/92, Main Shock

6.98 sec to 7.40 sec

(c) Average Time = 7.19 sec

—— 9281 kips/ft

– – – – 7000 kips/ft

Along West Abutment, 4/25/92, Main Shock

8.68 sec to 9.18 sec

(d) Average Time = 8.93 sec

—— 9340 kips/ft

– – – – 7000 kips/ft

Figure E-3. Individual loops for the spring along west abutment during the 1992 earthquake (continued)

52

Along West Abutment, 4/25/92, Main Shock

9.26 sec to   9.60 sec

(e) Average Time =   9.43 sec

——— 14136 kips/ft

– – – – – 13000 kips/ft

Along West Abutment, 4/25/92, Main Shock

11.08 sec to 11.48 sec

(f) Average Time = 11.28 sec
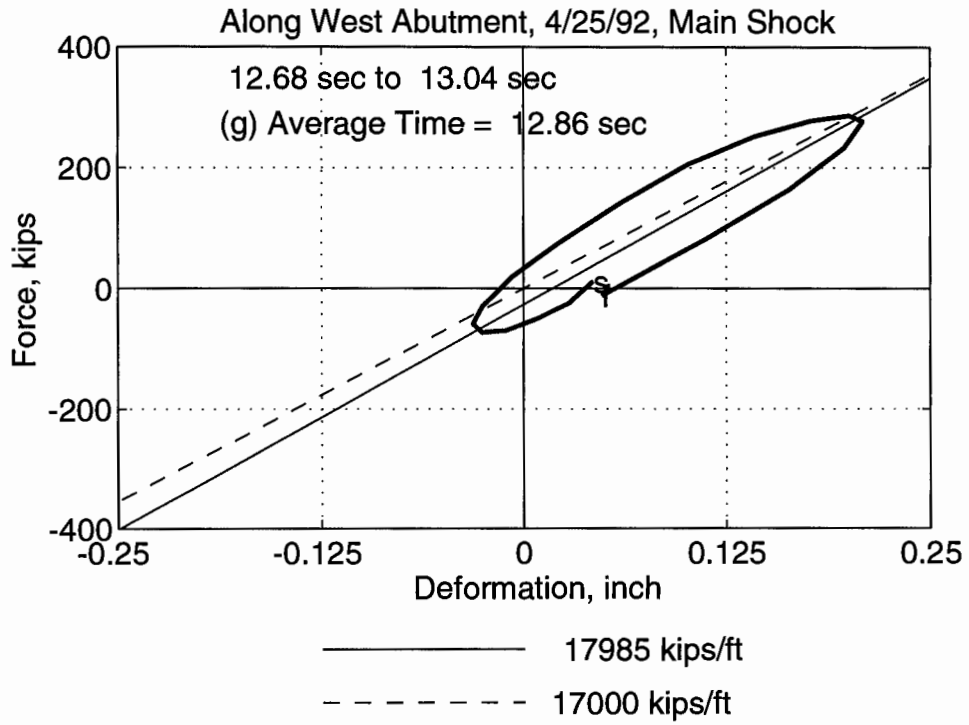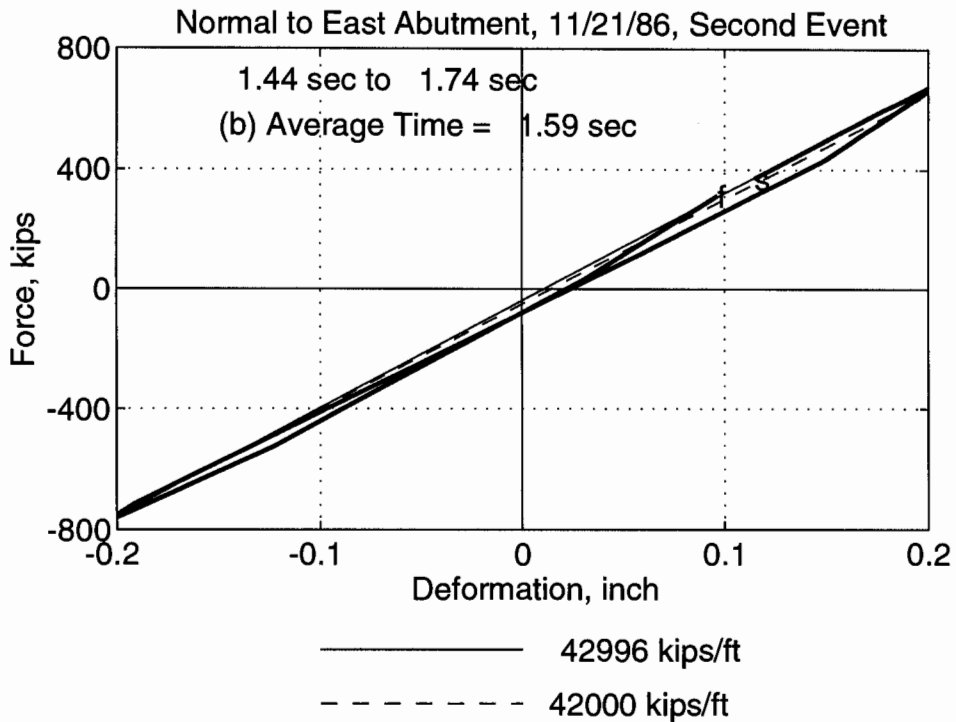
——— 18221 kips/ft

– – – – – 15000 kips/ft

Figure E-3. Individual loops for the spring along west abutment during the 1992 earthquake (continued)

53

Figure E-3. Individual loops for the spring along west abutment during the 1992 earthquake (continued)
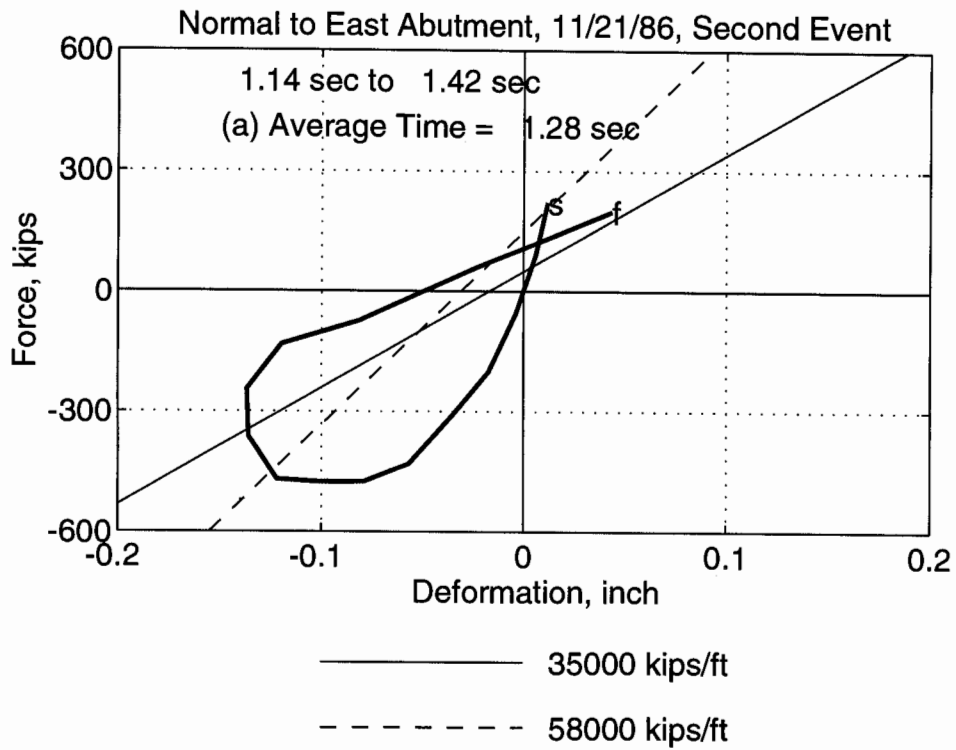
Figure E-4. Individual loops for the spring normal to east abutment during the 1986 earthquake
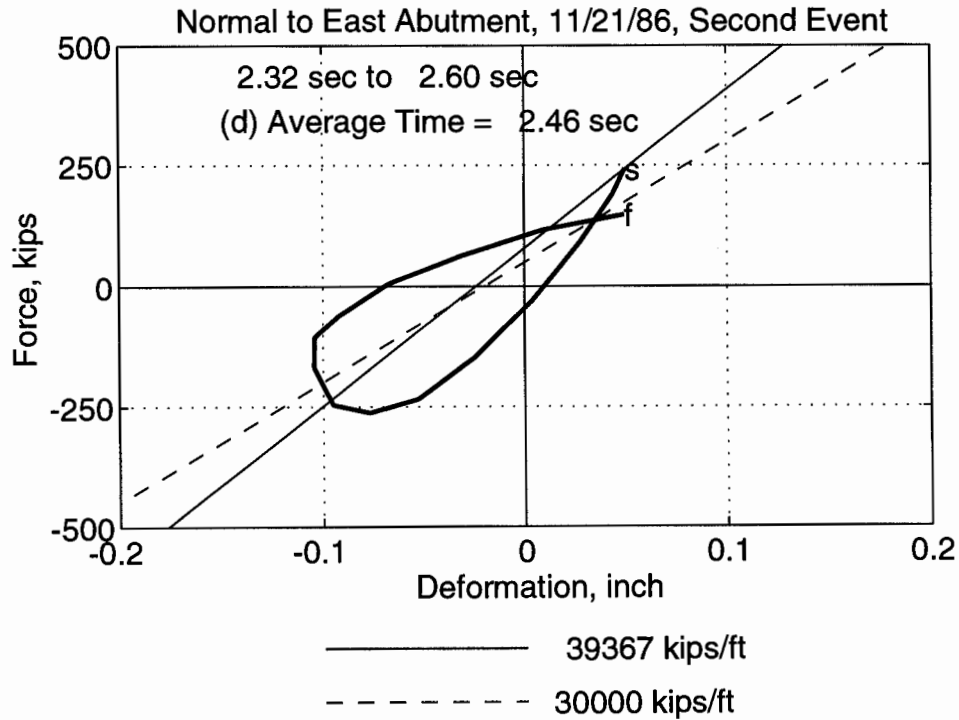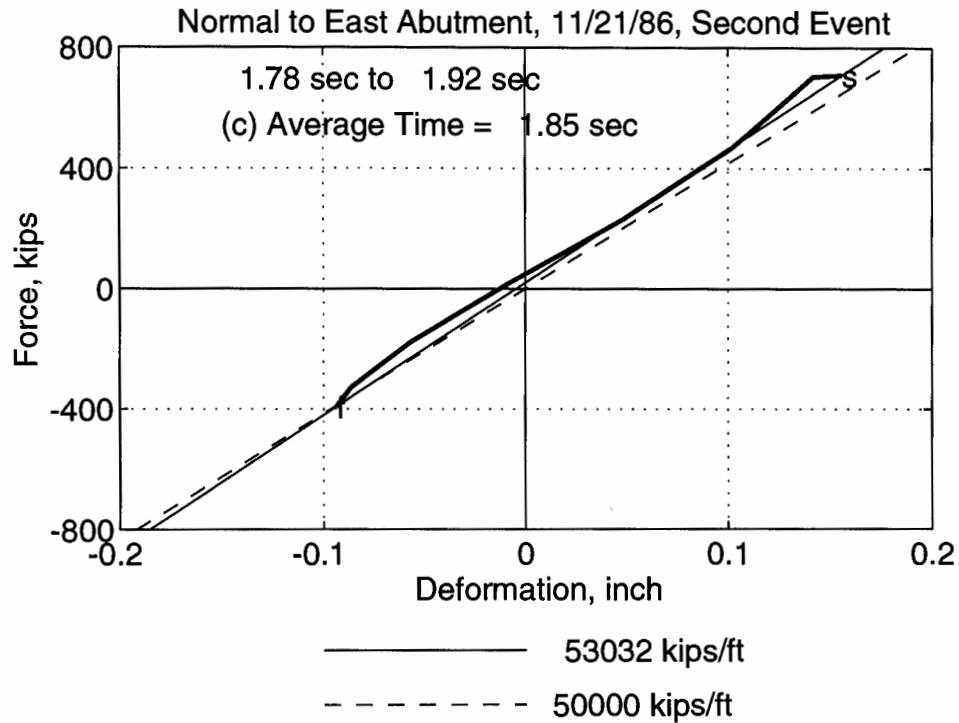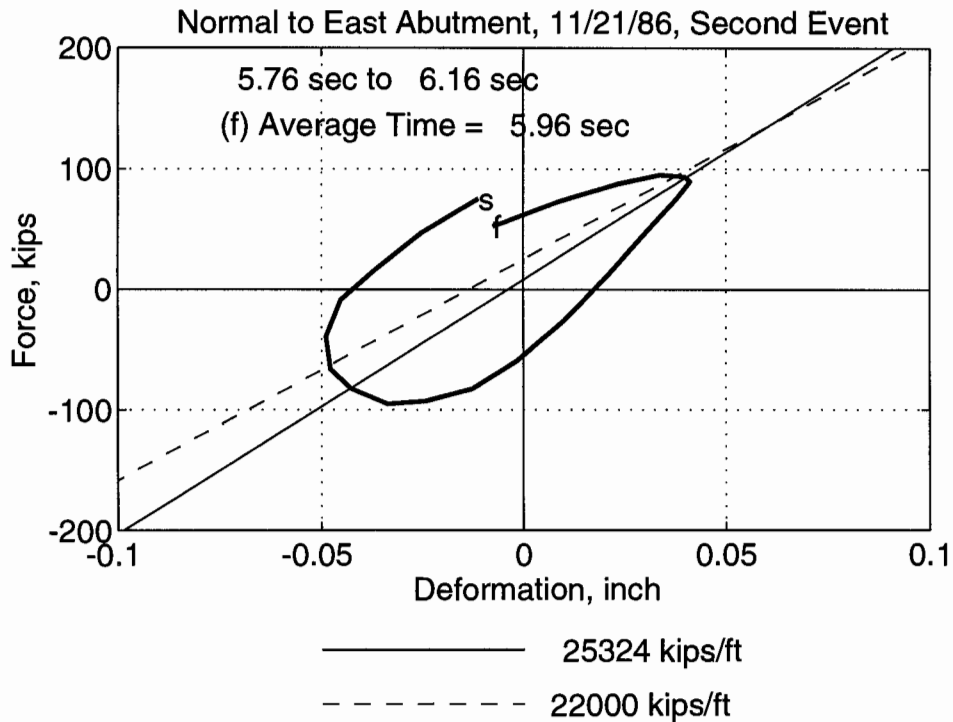
Figure E-4. Individual loops for the spring normal to east abutment during the 1986 earthquake (continued)

Normal to East Abutment, 11/21/86, Second Event

3.10 sec to 3.22 sec

(e) Average Time = 3.16 sec

Force, kips (y-axis): 400, 200, 0, -200, -400

Deformation, inch (x-axis): -0.1, -0.05, 0, 0.05, 0.1

——————— 35312 kips/ft

– – – – – – 38000 kips/ft

Normal to East Abutment, 11/21/86, Second Event

5.76 sec to 6.16 sec

(f) Average Time = 5.96 sec

Force, kips (y-axis): 200, 100, 0, -100, -200

Deformation, inch (x-axis): -0.1, -0.05, 0, 0.05, 0.1

——————— 25324 kips/ft
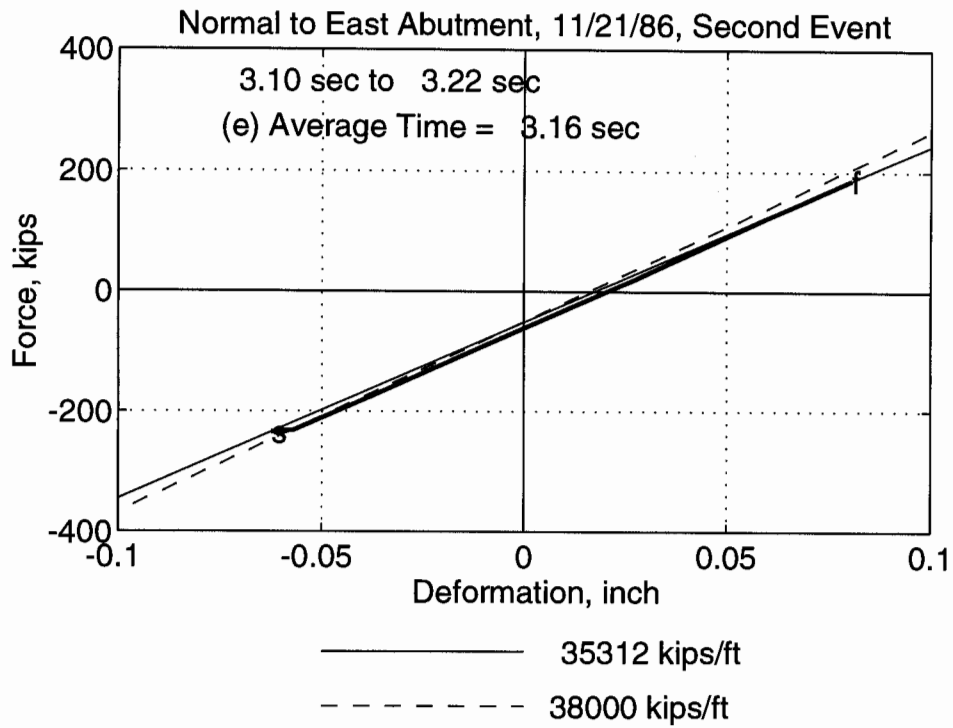
– – – – – – 22000 kips/ft

Figure E-4. Individual loops for the spring normal to east abutment during the 1986 earthquake (continued)
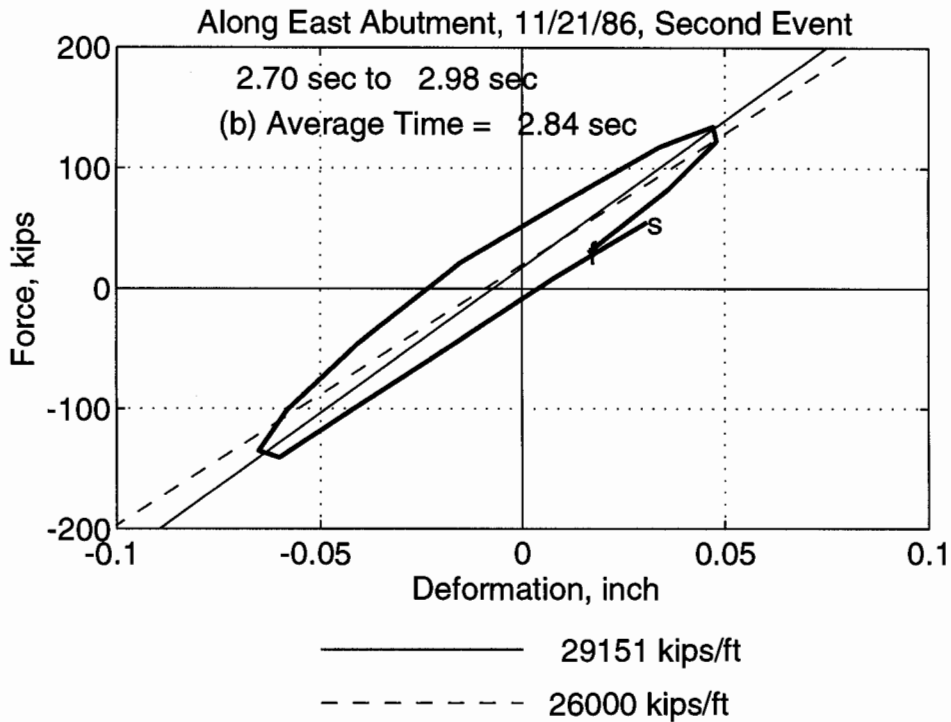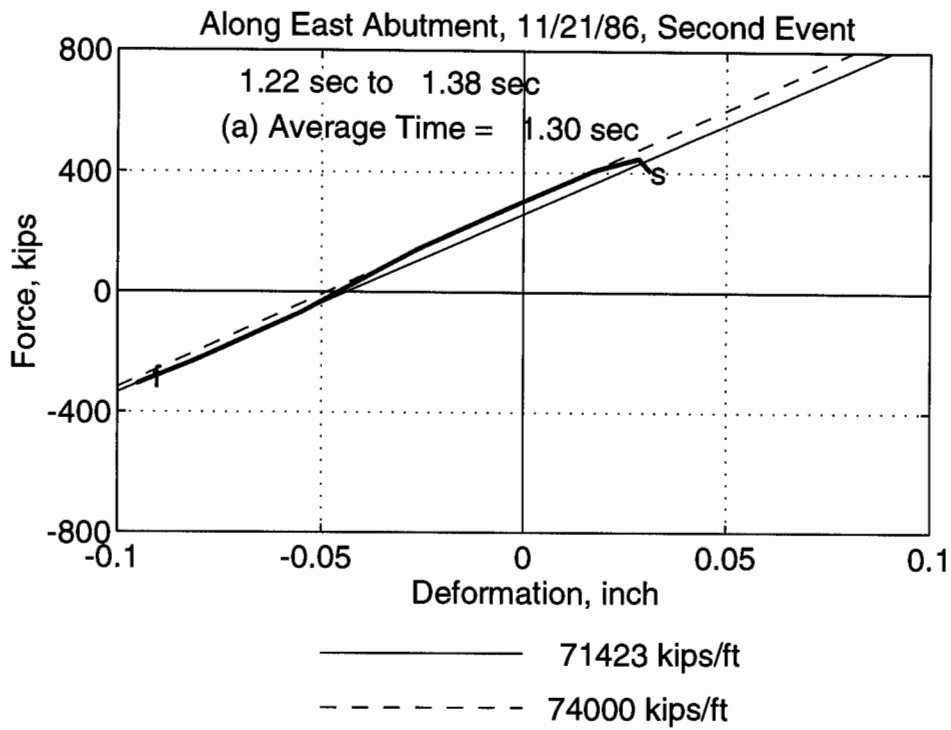
57

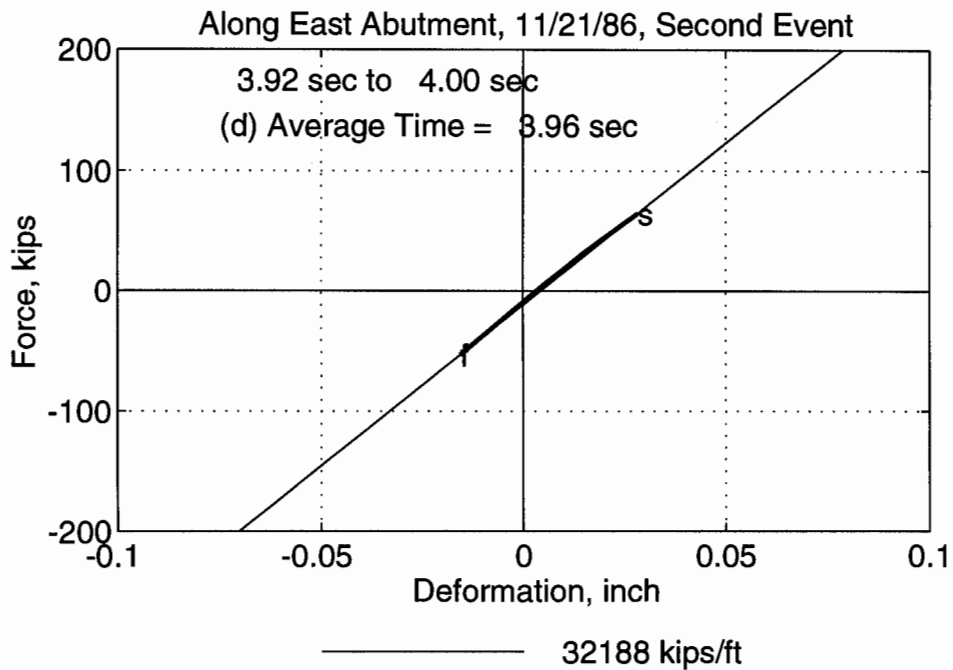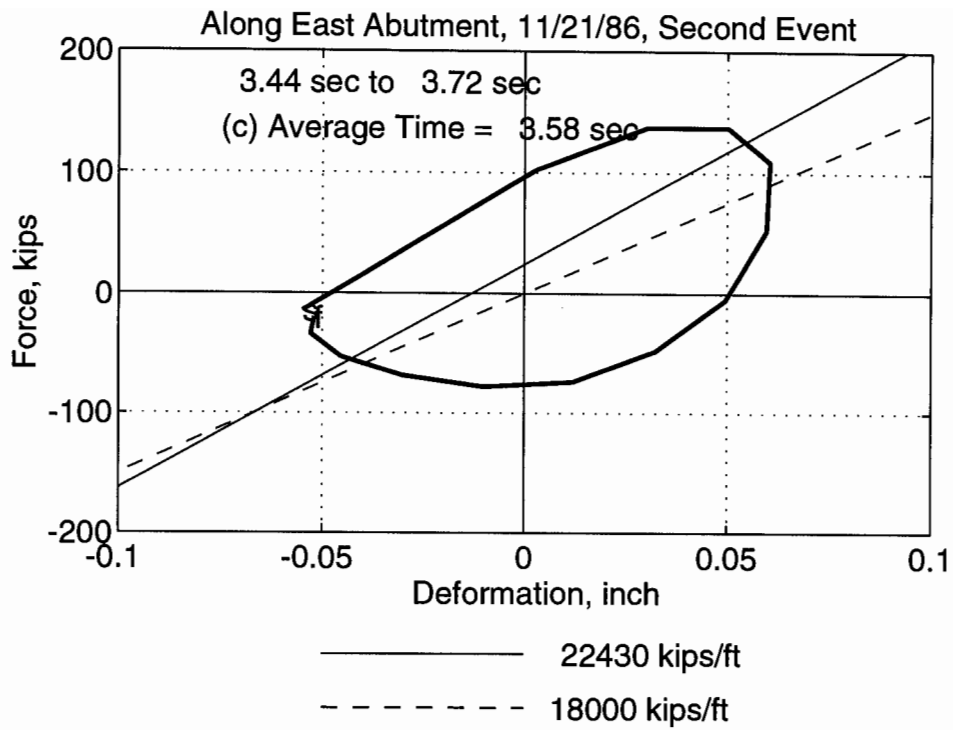Figure E-5. Individual loops for the spring along east abutment during the 1986 earthquake

Figure E-5. Individual loops for the spring along east abutment during the 1986 earthquake (continued)

Figure E-6. Individual loops for the spring along west abutment during the 1986 earthquake

Along West Abutment, 11/21/86, Second Event

2.60 sec to 2.90 sec
(c) Average Time = 2.75 sec

Force, kips

Deformation, inch

——— 52599 kips/ft
— — — — — — 45000 kips/ft

Along West Abutment, 11/21/86, Second Event

3.42 sec to 3.52 sec
(d) Average Time = 3.47 sec

Force, kips

Deformation, inch
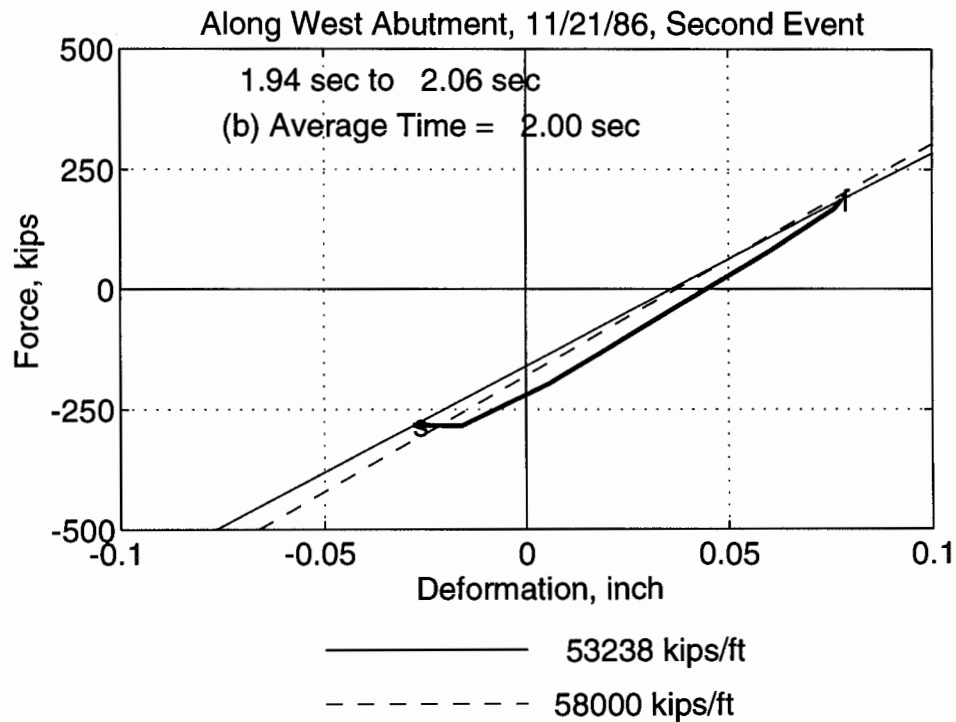
——— 39747 kips/ft
— — — — — — 45000 kips/ft

Figure E-6. Individual loops for the spring along west abutment during the 1986 earthquake (continued)
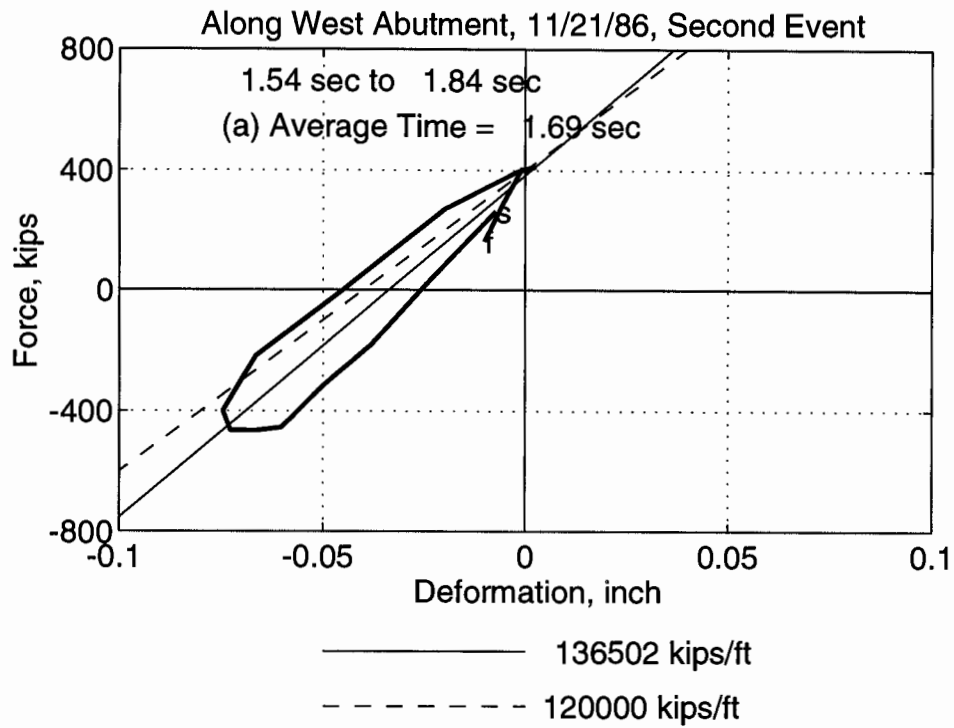
61

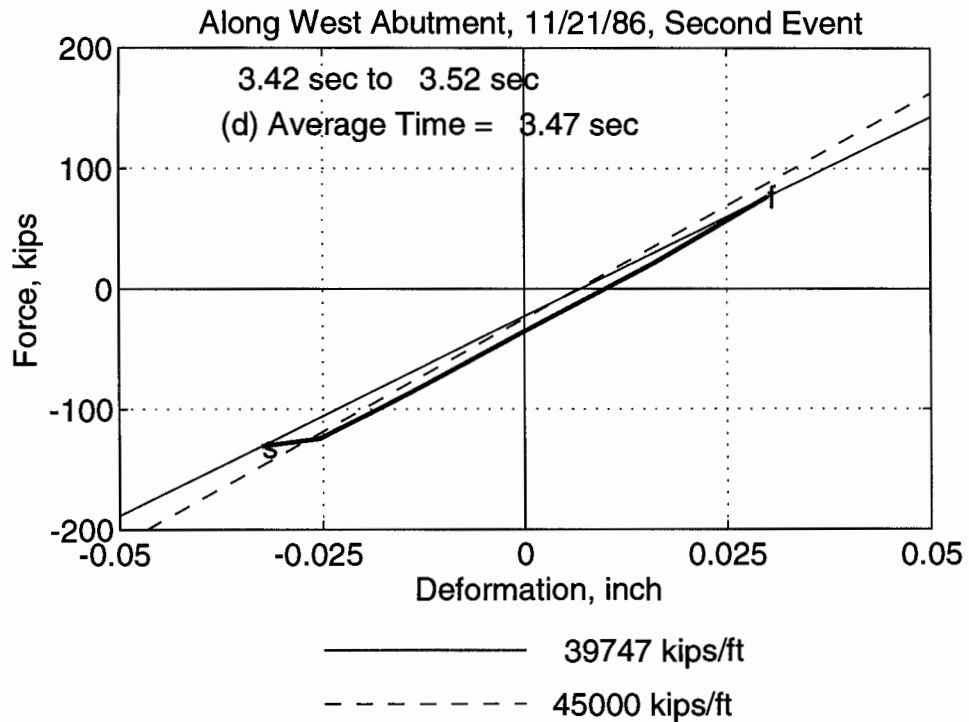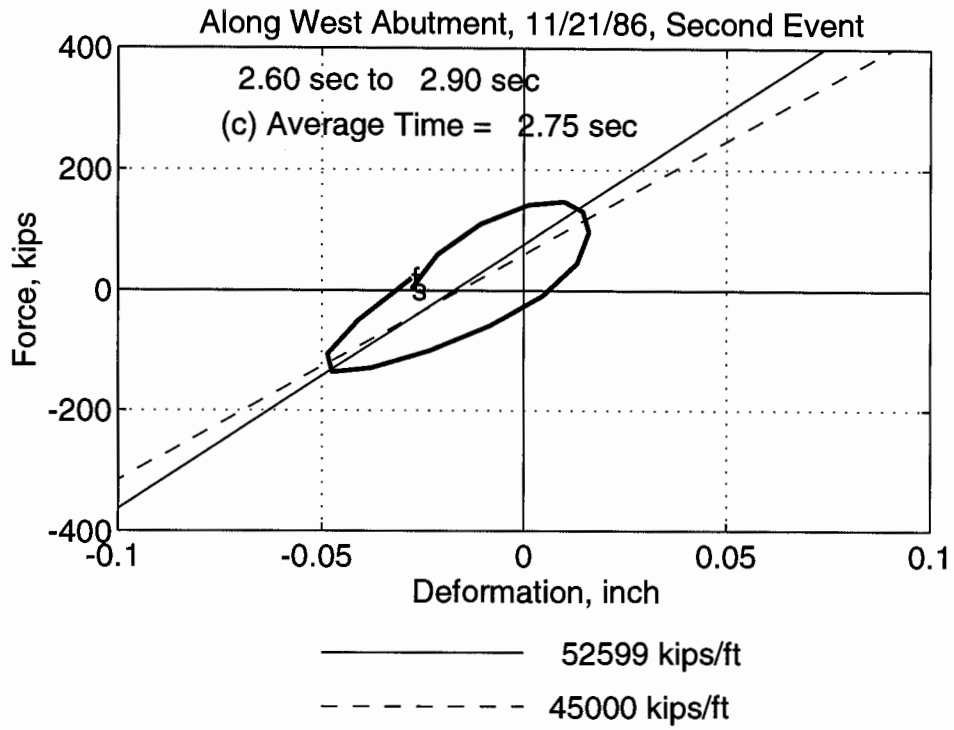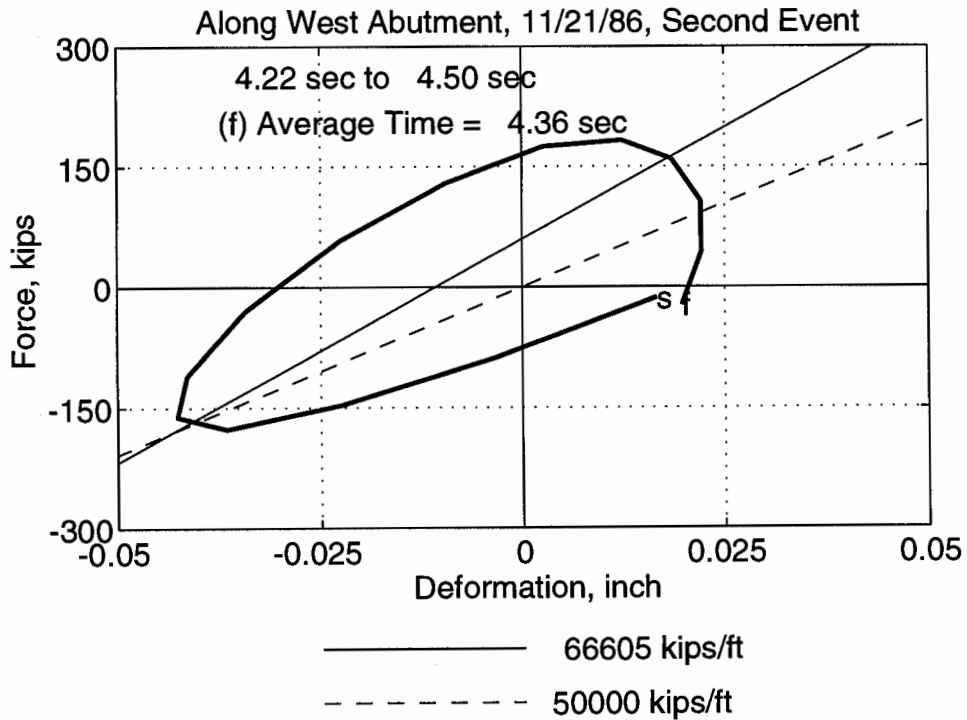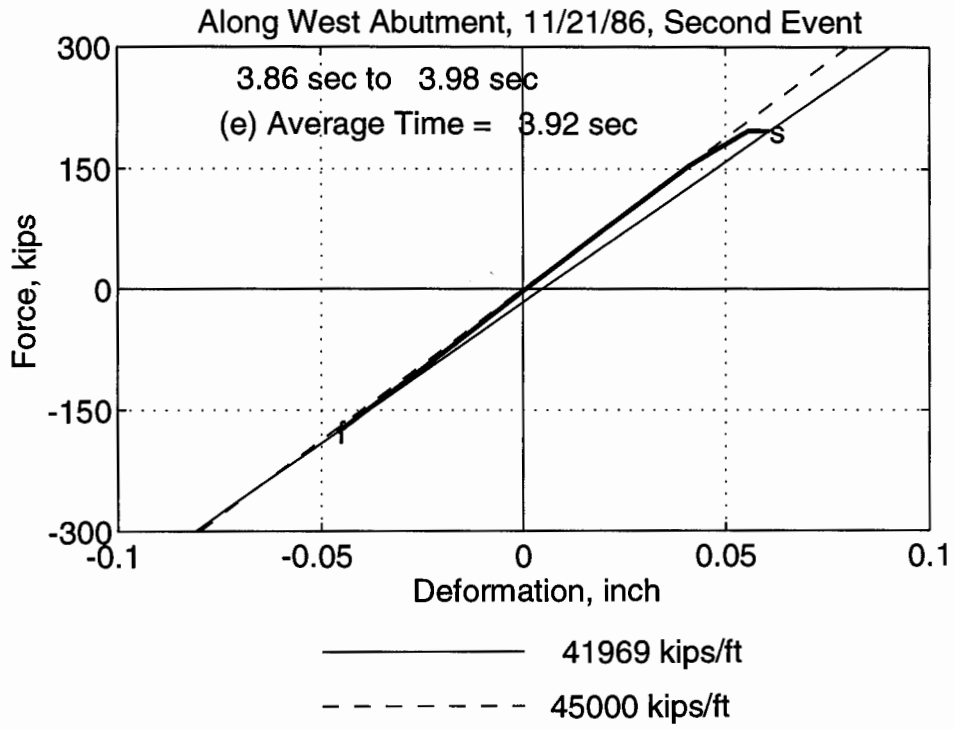Figure E-6. Individual loops for the spring along west abutment during the 1986 earthquake (continued)

Figure E-6. Individual loops for the spring along west abutment during the 1986 earthquake (continued)
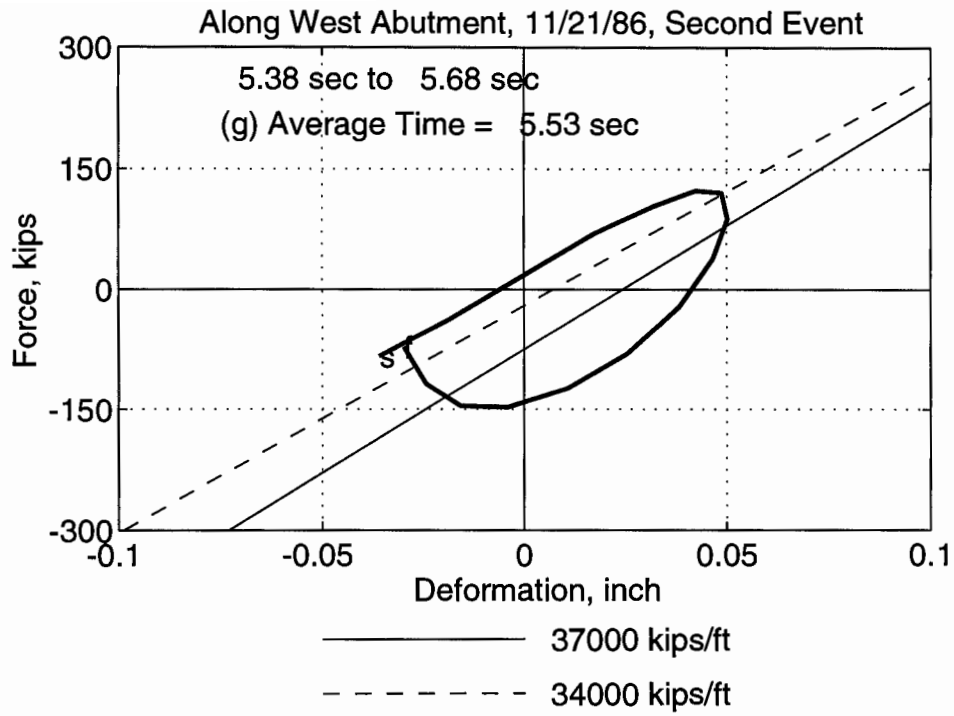
APPENDIX F: ABUTMENT STIFFNESS FROM CURRENT PROCEDURES

Presented in this appendix are the calculations for abutment stiffness using the current CALTRANS, AASHTO-83 and ATC-6 procedures. The stiffness values are compared in Figure 12 with the values determined from the recorded motions to evaluate the current procedures for modeling abutment stiffness. The results are presented first for the CALTRANS procedure followed by the AASHTO-83/ATC-6 procedure.

CALTRANS Procedure

The abutment stiffness is computed as the ratio of the abutment capacity, determined by the procedure presented in Memo 5-1 of CALTRANS (1988), and the acceptable deformation in the abutment. Since it is usually impractical to structurally size the abutment backwall below the soffit of the superstructure to totally mobilize the backfill, the abutment capacity is based on mobilizing the backfill only equal to the depth of the superstructure. The ultimate passive resistance of the backfill is assumed to be 7.7 kips per square foot; for backfill depth smaller than 8 feet, the resistance is reduced by a factor of $\sqrt{h/8}$ in which h is the actual depth of the backfill. The ultimate capacity of the Class 45 piles used in the abutment foundation of the US 101/Painter Street Overpass is assumed to be 40 kips. Both the backfill and the pile are assumed to reach their ultimate capacity at a deformation of one inch. Two values of the acceptable deformations are considered: 1 inch and 2.4 inch. The former of these two values corresponds to the deformation for which the soil behind the backwall of the abutment and the pile below the footing reach their ultimate resistance of 7.7 ksf and 40 kips, respectively. The latter value corresponds to the limiting value of the deformation for avoiding abutment damage; this value is based on the suggestion in Bridge Design Aids 14-1 of CALTRANS (1989). Note that the iterative procedure in which the initial stiffness of the abutment is based on the soil stiffness of 200 kips/inch per linear foot of the abutment backwall or wingwall (CALTRANS, 1989; Tsai et al., 1993) is not included in this investigations because CALTRANS engineers no longer use this procedure.

Longitudinal Stiffness

For each acceptable deformation level, the longitudinal stiffness is computed for several different abutment behaviors. The first two correspond to the case when the resistance is provided only by one abutment; this would occur either before closure of the expansion joint gap or after failure of the shear key at the west abutment. The other two correspond to the case when both abutments contribute to the total resistance; this would occur when the shear key is engaged at the west abutment. For each of the two cases, two possible failure modes are considered: shear failure in the backwall just below the soffit of the road deck before the piles in the foundation fail, and failure of piles before failure in the backwall. Presented next are the calculations for resistance in the longitudinal direction followed by the calculations of stiffness for the acceptable deformation.

Required in computing the abutment capacity for these different cases are the ultimate resistance of the soil, R_{SOIL}, shear capacity of the diaphragm, V_{DIA}, and resistance of the piles at the east and the west abutment, $R_{PILES,E}$, and $R_{PILES,W}$. These capacities are:

$R_{SOIL} = \left(\sqrt{h/8}\right)$ x 7.7ksf x Area $= \left(\sqrt{5.667/8}\right)$ x 7.7 ksf x (5.667 x 66.875) = 2455.66 kips

$V_{DIA} = \Phi_n\left(0.95\sqrt{f'_c}\right)$ x Area $= 0.85$ x $\left(0.95\sqrt{3500}\right)$ x (2.625 x 66.875) x 144 / 1000

$= 1207.65$ kips

$R_{PILES,E} =$ No. of Piles x 40kips = 14 x 40 = 560 kips

$R_{PILES,W} =$ No. of Piles x 40kips = 16 x 40 = 640 kips

The ultimate resistance of the abutment in the longitudinal direction corresponding to these cases are:

Case 1: $EQ_L = R_{SOIL} + V_{DIA} = 2455.66 + 1207.65 = 3663.31$ kips

Case 2: $EQ_L = R_{SOIL} + R_{PILES,E} = 2455.66 + 560 = 3015.66$ kips

Case 3: $EQ_L = R_{SOIL} + V_{DIA} + R_{PILES,E} = 2455.66 + 1207.65 + 560 = 4303.31$ kips

Case 4: $EQ_L = R_{SOIL} + R_{PILES,E} + R_{PILES,W} = 2455.66 + 560 + 640 = 3655.66$ kips

Dividing these abutment capacities by 0.2 ft (2.4 inch) leads to abutment stiffness of 18317, 15078, 21517, and 18278 kips/ft for the four cases, respectively. Similarly, dividing these

abutment capacities by 1/12 ft (1 inch) leads to stiffness values of 43960, 36188, 51640, and 43868 kips/ft for these cases.

Transverse Stiffness of East Abutment

Since the east abutment is integral with the footing, its ultimate capacity is calculated based on the shear capacity of one wingwall, V_{WW}, and resistance of piles, $R_{PILES,E}$. The shear capacity of one wingwall is:

$$V_{WW} = 0.85 \text{ x } (V_c + V_s) = 0.85 \text{ x } \left(0.95\sqrt{f'_c}\right) \text{ x Area} + 0.85 \text{ x } \frac{A_v f_y d}{S}$$

$= 0.85$ x 56.28 x $(0.75$ x 11.5 x $144) / 1000 + 0.85$ x $(2$ x $0.2)$ x 60 x $11.5/0.75 = 372.21$ kips

$EQ_T = V_{WW} + R_{PILES,E} = 372.21 + 560 = 932.21$ kips

Dividing this capacity with 0.2 ft (2.4 inch) leads to abutment stiffness of 4661 kips/ft. Similarly, the stiffness corresponding to 1 inch deformation is 11187 kips/ft.

Transverse Stiffness of West Abutment

Since the west abutment is seated on neoprene bearing, its ultimate capacity is calculated based on the shear capacity of one wingwall, V_{WW}, and capacity of the shear key. The shear key capacity is taken as 0.75 x $R_{PILES,W}$ (CALTRANS, 1988). The shear capacity of one wingwall is:

$$V_{WW} = 0.85 \text{ x } (V_c + V_s) = 0.85 \text{ x } \left(0.95\sqrt{f'_c}\right) \text{ x Area} + 0.85 \text{ x } \frac{A_v f_y d}{S}$$

$= 0.85$ x 56.28 x $(0.75$ x 12.34 x $144) / 1000 + 0.85$ x $(2$ x $0.2)$ x 60 x $12.34/0.75 = 399.40$ kips

$EQ_T = V_{WW} + 0.75 R_{PILES,W} = 399.40 + 0.75$ x $640 = 879.40$ kips

This capacity leads to abutment stiffness of 4397 kips/ft and 10553 kips/ft for acceptable deformation of 2.4 inch and 1 inch respectively.

AASHTO-83/ATC-6 Procedure

Following the procedure recommended by Lam and Martin (1986), the abutment stiffness in the longitudinal direction is computed as:

Stiffness = Stiffness due to Backfill + Stiffness Due to Piles = 0.425 x E_s x B + No. of Piles x 40 kips/inch per pile

Selecting $E_s = 1440$ ksf, and with B = 66.95 ft and 16 piles, the stiffness in the longitudinal direction is:

Stiffness = 0.425 x (1440 ksf) x 66.85 ft + 16 x (40 kips/inch x 12 inch/ft) = 48592 kips/ft

The transverse stiffness computed by using the same procedure with B = 13.2 ft, the effective length of the wingwall, is 15758 kips/ft.

LIST OF CSMIP DATA UTILIZATION REPORTS

California Department of Conservation
Division of Mines and Geology
Office of Strong Motion Studies
California Strong Motion Instrumentation Program (CSMIP)

The California Strong Motion Instrumentation Program (CSMIP) publishes data utilization reports as part of the Data Interpretation Project. These reports were prepared by investigators funded by CSMIP. Results obtained by the investigators were summarized in the papers included in the proceedings of the annual seminar. These reports and seminar proceedings are available from CSMIP at nominal cost. Requests for the reports, seminar proceedings and/or for additional information should be addressed to: Data Interpretation Project Manager, Office of Strong Motion Studies, Division of Mines and Geology, California Department of Conservation, 801 K Street, MS 13-35, Sacramento, California 95814-3531. Phone: (916)322-3105

CSMIP/92-01   **"Evaluation of Soil-Structure Interaction in Buildings during Earthquakes,"** by G. Fenves and G. Serino, June 1992, 57 pp.

CSMIP/92-02   **"Seismic Performance Investigation of the Hayward BART Elevated Section,"** by W. Tseng, M. Yang and J. Penzien, September 1992, 61 pp.

CSMIP/93-01   **"Influence of Critical Moho Reflections on Strong Motion Attenuation in California,"** by P. Somerville, N. Smith and D. Dreger, December 1993, 84 pp.

CSMIP/93-02   **"Investigation of the Response of Puddingstone Dam in the Whittier Narrows Earthquake of October 1, 1987,"** by J. Bray, R. Seed and R. Boulanger, December 1993, 60 pp.

CSMIP/93-03   **"Investigation of the Response of Cogswell Dam in the Whittier Narrows Earthquake of October 1, 1987,"** by R. Boulanger, R. Seed and J. Bray, December 1993, 53 pp.

CSMIP/94-01   **"Torsional Response Characteristics of Regular Buildings under Different Seismic Excitation Levels,"** by H. Sedarat, S. Gupta, and S. Werner, January 1994, 43 pp.

CSMIP/94-02   **"Degradation of Plywood Roof Diaphragms under Multiple Earthquake Loading,"** by J. Bouwkamp, R. Hamburger and J. Gillengerten, February 1994, 32 pp.

CSMIP/94-03   **"Analysis of the Recorded Response of Lexington Dam during Various Levels of Ground Shaking,"** by F. Makdisi, C. Chang, Z. Wang and C. Mok, March 1994, 60 pp.

CSMIP/94-04   **"Correlation between Recorded Building Data and Non-Structural Damage during the Loma Prieta Earthquake of October 17, 1989,"** by S. Rihal, April 1994, 65 pp.

CSMIP/94-05   **"Simulation of the Recorded Response of Unreinforced Masonry (URM) Infill Buildings,"** by J. Kariotis, J. Guh, G. Hart and J. Hill, October 1994, 149 pp.

CSMIP/95-01   **"Seismic Response Study of the Hwy 101/Painter Street Overpass Near Eureka Using Strong-Motion Records,"** by R. Goel and A. Chopra, March 1995, 70 pp.

SMIP89   "SMIP89 Seminar on Seismological and Engineering Implications on Recent Strong-motion Data," Preprints, Sacramento, California, May 9, 1989

SMIP90   "SMIP90 Seminar on Seismological and Engineering Implications on Recent Strong-motion Data," Preprints, Sacramento, California, June 8, 1990

SMIP91   "SMIP91 Seminar on Seismological and Engineering Implications on Recent Strong-motion Data," Preprints, Sacramento, California, May 30, 1991

SMIP92   "SMIP92 Seminar on Seismological and Engineering Implications on Recent Strong-motion Data," Proceedings, Sacramento, California, May 21, 1992

SMIP93   "SMIP93 Seminar on Seismological and Engineering Implications on Recent Strong-motion Data," Proceedings, Sacramento, California, May 20, 1993, 114 pp.

SMIP94   "SMIP94 Seminar on Seismological and Engineering Implications on Recent Strong-motion Data," Proceedings, Los Angeles, California, May 26, 1994, 120 pp.